Numerical and experimental study of molten pool behaviour and defect formation in multi-material and functionally graded materials laser powder bed fusion

Heng Gu[a,b*], Chao Wei[c], Lin Li[c], Michael Ryan[b], Rossitza Setchi[b], Quanquan Han[d], Lili Qian[e]

[a] School of Mechanical Engineering, Jiangsu University, Zhenjiang, Jiangsu 212013, China

[b] Cardiff School of Engineering, Cardiff University, Cardiff CF24 3AA, UK

[c] Laser Processing Research Centre, School of Mechanical, Aerospace and Civil Engineering, The University of Manchester, Manchester M13 9PL, UK

[d] School of Mechanical Engineering, Shandong University, Jinan 250061, China

[e] School of Energy and Power Engineering, Jiangsu University, Jiangsu 212013, China

Email: guheng@ujs.edu.cn

Abstract

Laser powder bed fusion (LPBF) of multi-material and functionally graded materials (FGM) has attracted significant research interest due to its ability to fabricate components with superior performance compared with those manufactured with single powder material. However, the forming mechanisms of various defects remain unknown. In this paper, a DEM-CFD model was first established to obtain an in-depth understanding of this process. It was discovered that the defects including partially melted and un-melted Invar36 powder were embedded in the lower level of the powder layer; this was attributed to the low laser absorptivity, low melting point and high thermal conductivity of the Cu10Sn powder. Inter-layer defects were more likely to occur with an increased powder layer thickness. In addition, the scanned track width was found related to an equilibrium achieved among the thermal properties of the powder mixture. Process parameters were optimised to obtain FGM structures without defects in both horizontal and vertical directions. Invar36/Cu10Sn samples were fabricated with a multi-material LPBF system using different mixed powder contents and laser volumetric energy densities (VEDs). By increasing the VED, fewer defects were observed

between the interface of two processed powder layers, which had a good agreement with the modelling results.

Keywords: Laser powder bed fusion (LPBF); Discrete element method (DEM); Computational fluid dynamics (CFD); Multi-material; Functionally graded materials (FGM)

1. Introduction

Laser powder bed fusion (LPBF) is an additive manufacturing process that fabricates three-dimensional components with complex features by scanning powder materials using a laser beam to melt and fuse the powder into a solid layer by layer [1, 2]. LPBF has many advantages over other additive manufacturing methods, including the ability to use an extensive range of materials, relatively low cost, increased functionality, and the fabrication of near-net-shaped parts ready to use [3]. Various powder materials, including metals, composites and ceramics, have been widely used for LPBF [4]. Recently, there has been growing interest in manufacturing parts using multi-material and functionally graded materials (FGM) LPBF. Multi-material LPBF processes multiple materials in the same layer or on different layers [5], while FGM LPBF is designed to allow a gradual structure and/or composition variation with respect to the location within the part [6]. Such structures combine the advantages of different materials to meet the multi-functional requirement for specific industrial applications [7].

Various LPBF systems have been developed to fabricate bimetallic components with dissimilar materials. Bai et al. [8] successfully manufactured interfaces of bimetallic 316L/C52400 using a multi-material LPBF system, and excellent interfacial metallurgical bonding was achieved. A recent study by Chen et al. [9] fabricated 316L/Cu10Sn bimetallic multi-material lattice structures, and found that re-melting could promote the mechanical strengthening of the fusion zone. A novel multi-material powder dispensing technique was adopted by Liu et al. [10] to produce bimetallic parts of 316L/C18400, and they observed the diffusion of Fe and Cu elements at the bonding interface of the two materials. Other bimetallic structures consisting of 316L/In718 [11], CuSn/18Ni300 [12], TiB_2/Ti6Al4V [13] and AlSi10Mg/C18400 [14] were successfully produced by various multi-material LPBF systems.

In addition to bimetallic structures, multiple materials processed both in the same and different layers has attracted considerable interest as it allows producing components with more

complexed features and FGM structures. Tey et al. [15] fabricated a 316L/Ti6Al4V multi-material component by applying Cu alloy as the interlayer during LPBF, and the critical interface was found at Cu alloy/Ti6Al4V which affected the strength of the part. An open-architecture LPBF system was developed by Nadimpalli et al. [16] to gradually change the sample composition from 316L to MS1 by mixing powders with controlled measures. Han et al. [17] manufactured Titanium/hydroxyapatite (Ti/HA) gradient samples with a quasi-continuously transitional method during LPBF, and they found that the addition of HA improved the hardness of the part while reduced the fracture hardness. Wei et al. [18] fabricated a part with anti-counterfeiting features by embedding Cu10Sn safety codes into metallic 316L components, and X-ray was found effective to identify these codes. Entangling structures consisting of hybrid of metals (Cu10Sn/316L) and a polymer (PA11) were manufactured by Chueh et al. [19] through a proprietary multiple-material LPBF system. A horizontal FGM structure of TiAl/ (α + β) titanium alloy was manufactured by Zhou et al. [20] during the electron beam powder bed fusion process. A multi-graded LPBF study of Ti6Al4V and In718 was conducted by Scaramuccia et al. [21] using a novel multi-material powder delivery strategy. Rankouhi et al. [22] employed a machine learning method to predict the suitable process parameters for manufacturing 316L/Cu multi-material part with a compositional gradient during LPBF. A recent investigation by Zhang et al. [23] employed a nozzle-based multi-material LPBF system to fabricate FGM components with a compositional change from Cu10Sn to glass, and a reduced ductility was found when transiting from metal to glass.

Significantly, the above-mentioned and related studies have reported many defects during the multi-material and FGM LPBF processes. For example, when manufacturing metal/glass multi-material components using a selective powder dispensing platform, Zhang et al. [24] discovered that some glass powder was sintered rather than melted both at the edge and in the body of the heat affected zone. Wei et al. [25] also observed some un-melted spherical 316L powder embedded in the Cu10Sn matrix when processing a functionally graded 316L/Cu10Sn

component. An increased number of pores was found by Chueh et al. [26] when increasing the volume fraction of the filling powder during the fabrication of functionally graded polymer/ceramic and polymer/metal structures by adopting a multi-material LPBF system equipped with ultrasonic vibration.

In addition to the experimental investigations, numerical modelling has been widely employed to help understand the complicated mechanisms involved in LPBF, which are often challenging to observe in real time. For multi-material LPBF simulation, the discrete element method (DEM) was adopted by Tan [27] to compare the heat transfer process between 316L and Ti6Al4V powders, and he discovered that the thermal conductivity difference of the two materials would have big influence on the temperature distribution of the powder bed. Dai and Gu [28] developed a volume of fluid (VOF) model to investigate the impact of laser energy density when processing TiC/AlSi10Mg powders in LPBF, and they found that poor surface quality would be obtained when applying both too high and too low laser energy densities. The molecular dynamic (MD) method was used by Sorkin et al. [29] to examine the melting and solidification behaviour of Fe/Al multi-material powders during multi-layer LPBF process, and they stated that insufficient energy input could lead to layer delamination. A DEM-CFD modelling framework was developed by Gu et al. [30] to study the track morphology and molten pool development during multi-material LPBF of 316L/Cu10Sn, and the phase diffusion of the two materials was found related to the Marangoni convection flow. Similarly, a recent study from Sun et al. [31] built a DEM-CFD model to evaluate the effect of mixed material content of IN718/Cu10Sn on the track formation during multi-material LPBF process. Numerical simulation was also adopted to reveal the mechanisms by which defects form. For example, Tang et al. [32] studied the forming mechanisms of near-spherical and irregularly shaped pores in LPBF, and they reported that the wetting behaviour of the molten material would determine the morphology of the scanned track. Other defects, including inter-track/inter-layer voids, balling effect and track nonuniformity, were also examined by

investigating the impact of the scanning strategy and the hatch spacing [33]. However, previous simulation work on the formation of defects in LPBF only focuses on the processing of one material at a time.

Despite the fact that many studies have been conducted on multi-material and FGM LPBF, no detailed investigation into the formation of defects during this process has been reported. In addition, no previous study has employed simulation methods to obtain an in-depth understanding of defect formation when processing multiple powder materials with multiple scanning passes and layers.

This study uses numerical and experimental methods to examine the formation of defects during the multi-material and FGM LPBF processing of Invar36/Cu10Sn parts. An integrated modelling framework was adopted to help understand the track morphology and molten pool dynamics in the multi-material LPBF process. By analysing the simulated temperature distribution and the molten pool volume history of different cases, the impacts of various process parameters, including laser power, layer thickness and hatch spacing, on the formation of inter-layer/inter-track defects, were examined. Defects, including partially and un-melted powder particles, spherical and non-spherical porosity, balling effect, isolated clusters and lack of fusion, were studied for multi-layer, multi-track, and multi-material LPBF processes. In addition, simulations of FGM in both horizontal and vertical building directions were performed, and process parameters were optimised to achieve FGM structures without defects. To compare with the modelling results, samples with different material contents were fabricated using different process parameters on a modified multi-material LPBF system. A good agreement was obtained between the simulated and experimental results.

2. Simulation mathematical formulation

A DEM-CFD framework was established to model the complex mechanisms involved in the LPBF process, which include the deposition of multiple powder materials and laser-powder interaction.

2.1 Simulation of powder deposition

The model of the multi-material powder deposition with different material contents was developed using the discrete element method (DEM) [34]. Powder particles with different mixture contents were first generated from a plane above the substrate with required powder layer thickness, and the powder would fall freely under gravity. A rigid plane was then employed to compress the powder layer to simulate the pressure implemented by the recoater blade during experiments in order to increase the powder packing density. After deposition, the powder information including the diameter and location were exported.

The translational and rotational motion of each powder particle is determined by Newton's second law, and the detailed DEM governing equations are described in Ref. [35]. For contact forces considered in this model, the non-linier Hertz-Mindlin model [36] was applied to simulate the interaction between the powder particles. The tangential force F_t, tangential damping force F_t^d, normal force F_n and normal damping force F_n^d can be calculated using the equations (1):

$$\begin{cases} F_t = -8G^*\sqrt{R^*\delta_n}\delta_t \\ F_t^d = -2\sqrt{\frac{5}{6}}\frac{lne}{\sqrt{ln^2e+\pi^2}}\left(8G^*\sqrt{R^*\delta_n}m^*\right)^{\frac{1}{2}}\overrightarrow{v_t^{rel}} \\ F_n = \frac{4}{3}E^*\sqrt{R^*}\delta_n^{\frac{3}{2}} \\ F_n^d = -2\sqrt{\frac{5}{6}}\frac{lne}{\sqrt{ln^2e+\pi^2}}\left(2E^*\sqrt{R^*\delta_n}m^*\right)^{\frac{1}{2}}\overrightarrow{v_n^{rel}} \end{cases} \quad (1)$$

where δ_t and δ_n are the tangential and normal overlap respectively, $v_t^{\overrightarrow{rel}}$ and $v_n^{\overrightarrow{rel}}$ define the tangential and normal component of the relative velocity, e represents the restitution coefficient. The tangential force F_t is limited by friction force $\mu_s F_n$, where μ_s is the friction coefficient. The equivalent properties including radius R^*, Young's modulus E^*, shear modulus G^* and mass m^* are presented in equations (2) [37]:

$$\begin{cases} R^* = \dfrac{r_1 r_2}{r_1 + r_2} \\ m^* = \dfrac{m_1 m_2}{m_1 + m_2} \\ E^* = \dfrac{E_1 E_2}{(1-\xi_2^2)E_1 + (1-\xi_1^2)E_2} \\ G^* = \dfrac{G_1 G_2}{(1-\xi_2^2)G_1 + (1-\xi_1^2)G_2} \end{cases} \tag{2}$$

where r_1 and r_2, m_1 and m_2, G_1 and G_2, and ξ_1 and ξ_2 are the radii, masses, Young's moduli, shear moduli, and Poisson ratios of the two contacting powder particles, respectively. To account for the influence of attractive forces between fine powders, the JKR cohesion model which was originally implemented for Van Der Waals forces was used, which is defined in equation (3) [36]:

$$F_{JRK} = -4\sqrt{\pi \gamma_s E^*} a^{\frac{3}{2}} + \frac{4E^*}{3R^*} a^3 \tag{3}$$

where γ_s is the surface energy density. A commercial software, EDEM [36], was employed for the multi-material powder deposition simulations. The Rayleigh critical time-step limit [38] was applied in order to ensure stability, which was given by equation (4):

$$\Delta t < \frac{\pi R_{min} \sqrt{\dfrac{\rho}{E}}}{0.163\xi + 0.877} \tag{4}$$

Invar36 and Cu10Sn were used as the two powder materials in this study. Invar36 is a 36% nickel-iron alloy which is widely applied as a high precision and highly reliable material in

industries such as aerospace engineering and precision instruments, due to its extremely low thermal expansion coefficient [39]. Cu10Sn is a copper-tin alloy with 10% Sn content which has been widely used in manufacturing electrical connections and heat exchangers, owing to its excellent thermal and electrical conductivities [40]. Combinations of Invar36 and copper alloys have been used extensively for high-density printed circuits [41], by utilizing the advantages of the low thermal expansion of Invar36, and high electrical and thermal conductivities of copper alloys. In order to compare with the experimental investigation, the powder size distribution used in the experiments was first examined by Malvern UK Mastersizer 3000 particle size analyser. Invar36 and Cu10Sn powder were provided by LPW Technology Ltd., UK and Makin Metal Powders Ltd., UK, respectively. The powder sizes of D10, D50 and D90 were measured as 18.1 μm, 31.2 μm and 53.4 μm for Invar36, and 17.9 μm, 30.9 μm and 53.2 μm for Cu10Sn, respectively. The powder distributions obtained from the analyser were imported into DEM simulation as normal distribution functions. After calculation, the simulated powder sizes of D10, D50 and D90 were 18.0 μm, 31.0 μm and 53.7 μm for Invar36, and 17.9 μm, 30.6 μm and 51.5 μm for Cu10Sn.

The material properties of Invar36 and Cu10Sn powder used in DEM modelling are presented in Table 1. Properties including Poisson ratio, surface energy density and friction coefficient of Cu10Sn powder were obtained from literature [42, 43]. Due to the limitation of existing experimental data, the properties of Invar36 were used as the same properties of general steel granules [44]. Young's modulus of both powder particles were adopted two orders less than the real value in order to increase the limit of Rayleigh critical time-step [45], which was 3×10^{-8} s in this study.

Table 1. Material properties of Invar36 and Cu10Sn used in DEM modelling

Symbol	Nomenclature	Value	Powder
ρ	Density (kg·m^{-3})	8050	Invar36

		8780	Cu10Sn
E	Young's modulus (MPa)	1.4×10^3	Invar36
		1.1×10^3	Cu10Sn
ξ	Poisson ratio	0.3	Invar36
		0.33	Cu10Sn
e	Restitution coefficient	0.9	Invar36
		0.3	Cu10Sn
μ_s	Friction coefficient	0.62	Invar36-Invar36
		0.3	Cu10Sn-Cu10Sn
		0.5	Invar36-Cu10Sn
γ_s	Surface energy density (mJ/m^2)	0.097	Invar36
		0.25	Cu10Sn

2.2 Simulation of laser-powder interaction

After obtaining the powder information from EDEM, computational fluid dynamics (CFD) was adopted to calculate the laser-powder interaction. A three-dimensional transient model was developed, with the fluid flow treated as laminar, Newtonian and incompressible [46]. Fig.1 illustrates the schematic and boundary conditions of the model.

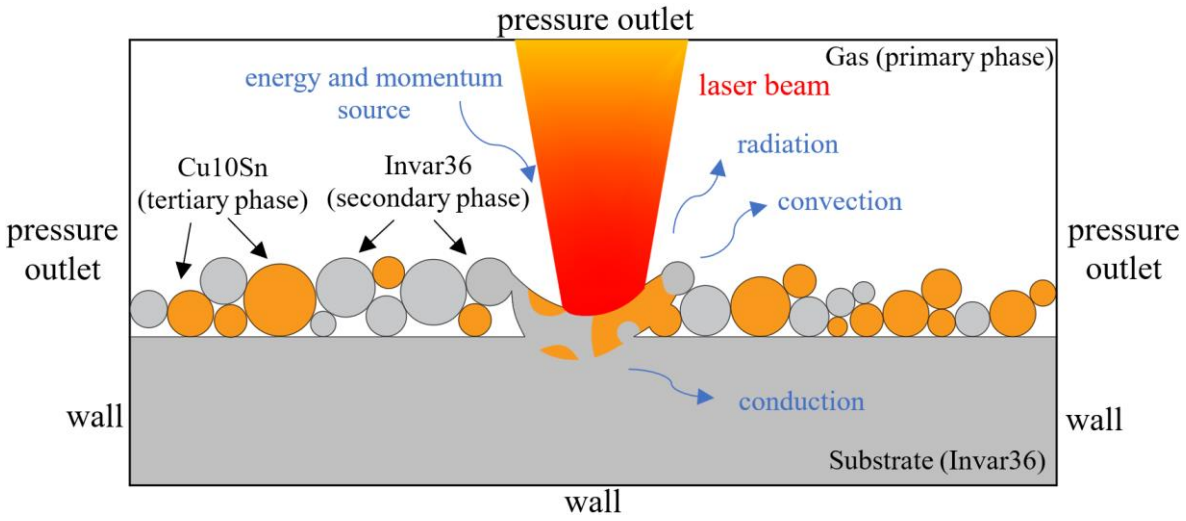

Fig. 1. Schematic and boundary conditions of the model

The continuity, momentum and energy equations of the CFD model are formulated in the equations (5-7) [47] shown below:

$$\frac{\partial \rho}{\partial t} + \nabla \cdot (\rho \vec{v}) = 0 \tag{5}$$

$$\frac{\partial}{\partial t}(\rho \vec{v}) + \nabla \cdot (\rho \vec{v} \vec{v}) = -\nabla p + \nabla \cdot [\mu(\nabla \vec{v} + \nabla \vec{v}^T)] + \rho \vec{g} + M_s + M_r + M_{st} \tag{6}$$

$$\frac{\partial (\rho H)}{\partial t} + \nabla \cdot (\rho \vec{v} H) = \nabla \cdot (\lambda \nabla T) + E_h \tag{7}$$

where $\vec{v}$ represents the fluid velocity, ρ is the material density, λ defines the thermal conductivity, H is the material enthalpy, p is the pressure, μ represents the dynamic viscosity, f is the liquid fraction, $\vec{g}$ represents the gravitational acceleration, M_s defines the momentum sink, M_r represents the recoil pressure, M_{st} is the surface tension force and E_h is user-defined heat source. Enthalpy-porosity method [48, 49] was employed to model the melting and solidification process of the powder particles. The material enthalpy was given by:

$$H = h_{ref} + \int_{T_{ref}}^{T} C_p dT + fL \tag{8}$$

where h_{ref} represents the reference enthalpy, T_{ref} defines the reference temperature, C_p is the specific heat, L represents the latent heat of the material. Liquid fraction f has a value ranging between 0 and 1 which indicates the fraction of liquid in a control volume. A momentum sink M_s was defined to extinguish the fluid velocity in the mushy zone during the solidification process, which is expressed in equation (9):

$$M_s = \frac{(1-f)^2}{(f^3+\varepsilon)} A_{mush} \vec{v} \tag{9}$$

where A_{mush} is mushy zone constant and ε is a small constant to prevent division by zero.

The rapid development of the free surface was captured by implementing the VOF [50] method. Two metal phases (Invar36 and Cu10Sn), as well as a gas phase (air), were defined in VOF. User defined functions (UDF) were used to track the volume fractions of these three phases inside an element defined as: C_VOF(c,pri_th), C_VOF(c,sec_th) and C_VOF(c,ter_th). By tracking and comparing these three values (ranging from 0~1), the free surface between air and Invar36, as well as air and Cu10Sn could be distinguished separately. After identifying the material type of the free surface, the laser absorptivity was applied accordingly per control volume. The conservation of the volume fraction *F* is given by equation (10) [50]:

$$\frac{\partial F}{\partial t} + \nabla \cdot (\vec{v} F) = 0 \tag{10}$$

After capturing the free surface, a user-defined Gaussian distributed volumetric energy source E_h was applied to the molten pool free surface. With the rapid development of the molten pool profile, the amount of total heat input applied on the free surface would vary between two time-steps due to the change of element number on the free surface. Therefore, a self-adaptive Gaussian distributed heat source was developed to keep the conservation of total heat input between different moments. The number of elements *n* located on the evolving

molten pool within the laser beam radius was first computed and the volumetric heat source E_h is defined in equation (11) [30]:

$$E_h = \frac{P_{laser} * \eta}{V_{element} * \sum_1^n \exp\left(-\frac{3 * r_n^2}{r^2}\right)} * \exp\left(-\frac{3 * r_n^2}{r^2}\right) \quad (11)$$

where P_{laser} is the laser power, η defines the laser absorptivity, r represents the laser beam radius, $V_{element}$ is the element volume, r_n represents the distance between the element and the laser beam centre.

The recoil pressure, which occurs due to vaporization of material, was included in the momentum equation, and is expressed in equation (12) [51]:

$$M_r = 0.54 P_0 exp\left(\Delta H_{vap} \frac{T - T_{vap}}{RTT_{vap}}\right) \quad (12)$$

where P_0 is the environmental pressure, ΔH_{vap} defines the latent heat of vaporization, T_{vap} represents the vaporization temperature and R defines the ideal gas constant.

Surface tension force plays a significant role in the molten pool evolvement during LPBF process. Two surface tension forces including the Marangoni shear stress and the surface tension force normal to the gas/metal free surface were applied on the molten pool, which is given in equation (13) [52]:

$$M_S = M_{sm} + M_{sn} = \nabla_t \sigma + \sigma \cdot \kappa \cdot \vec{n} \quad (13)$$

where ∇_t indicates the gradient operator tangent to the interface, σ is the surface tension, κ represents the interfacial curvature and $\vec{n}$ is the unit vector normal to the interface. Boundary conditions, including thermal conduction, convection and radiation, were added to the substrate surfaces defined as walls, while the external boundaries of the air phase were defined as pressure outlets.

After establishing the model, all the conservation equations were solved in ANSYS Fluent v18.2, using a pressure-based transient solver. The dimensions of the calculation domain were 300 μm × 1000 μm × 180 μm, and the model contained 432,000 hexahedral elements with uniform grid spacing of 5 μm. The calculation time-step was adopted as 1×10^{-6} s, and it took approximately 18 hours to simulate one scanning track of 5.353 ms using a desktop equipped with Intel Core i9-9900K CPU (3.6 GHz) and 32 GB RAM. Table 2 lists the thermo-physical properties of the two materials used in this study, which include solidus and liquidus data [53] and surface tension information [54] for Invar36, as well as solidus and liquidus properties [55] and surface tension data [56] for Cu10Sn. The laser absorptivity of the powder was calculated based on a ray-tracing model developed by Boley et al. [57].

Table 2. Thermo-physical properties of Invar36 and Cu10Sn used in CFD modelling

Symbol	Nomenclature	Invar36	Cu10Sn
ρ_s	Solidus density (kg·m^{-3})	8060.8-0.4367T	8780
ρ_l	Liquidus density (kg·m^{-3})	8289.1-0.7083T	7700
T_s	Solidus temperature (K)	1690	1053
T_l	Liquidus temperature (K)	1698	1278
k_s	Solidus thermal conductivity (W·m^{-1}·K^{-1})	4.527+0.0148T	46
k_l	Liquidus thermal conductivity (W·m^{-1}·K^{-1})	6.206+0.01264T	64
μ	Viscosity (kg·m^{-1}·s^{-1})	$10^{(2344.2/T-3.5876)}$	0.00225
σ	Surface tension (kg·s^{-2})	1.93	1.15
$d\sigma/dt$	Surface tension coefficient (kg·s^{-2}·K^{-1})	-0.173×10^{-3}	−0.2×10^{-3}
L_m	Latent heat (J·kg^{-1})	2.76×10^5	1.958×10^5
C_p	Heat capacity (J·kg^{-1}·K^{-1})	801	505
η	Laser absorptivity	0.6	0.17

A locally homogeneous mixture approach [58] was adopted to compute the change of material properties due to mixing of the materials, where the mixture properties were determined by the volume fraction of the component phases in a control volume. Properties including material density, surface tension, viscosity, laser absorptivity and thermal conductivity were calculated based on the volume-averaged method, which is described as:

$$\varphi_{mix} = \sum_{i=1}^{n} F_i \, \varphi_i \tag{14}$$

where φ_{mix} represents the mixed material property, F_i is the volume fraction of component phase i and φ_i is the component material property. Other material properties including melting/solidification temperature, latent heat and heat capacity were calculated using the weight-averaged method, which is given in equation (15):

$$\varphi_{mix} = \frac{\sum_{i=1}^{n} F_i \, \rho_i \varphi_i}{\sum_{i=1}^{n} F_i \, \varphi_i} \tag{15}$$

3. Simulation results and discussion

3.1 Model validation

A multi-material LPBF system [5] developed at The University of Manchester was employed to validate the model. The system is equipped with a continuous wave fibre laser (IPG Photonics, YLR-500-WC) of 1070 nm wavelength and 500 W laser power. The laser beam is focused at 254 mm focal distance with a spot size of 80 μm. A Y-shape powder blender was used to mix the powder and obtain a homogeneous distribution of the mixed powder with different compositions. Different laser powers and scanning speeds were applied to conduct single-track experiments for mixed powder of three compositions: pure Invar36, 50 vol% Invar36, and pure Cu10Sn. Fig. 2(a) presents the macroscopic results of the scanned tracks using different process parameters and mixed powder contents. An SEM (Zeiss Sigma VP FEG

SEM) was employed to reveal the morphology of the scanned tracks. Fig. 2(b), (d) and (f) show the single-track image for pure Invar36, 50 vol% Invar36 and pure Cu10Sn respectively, with 250 W laser power and 150 mm/s laser scanning speed applied.

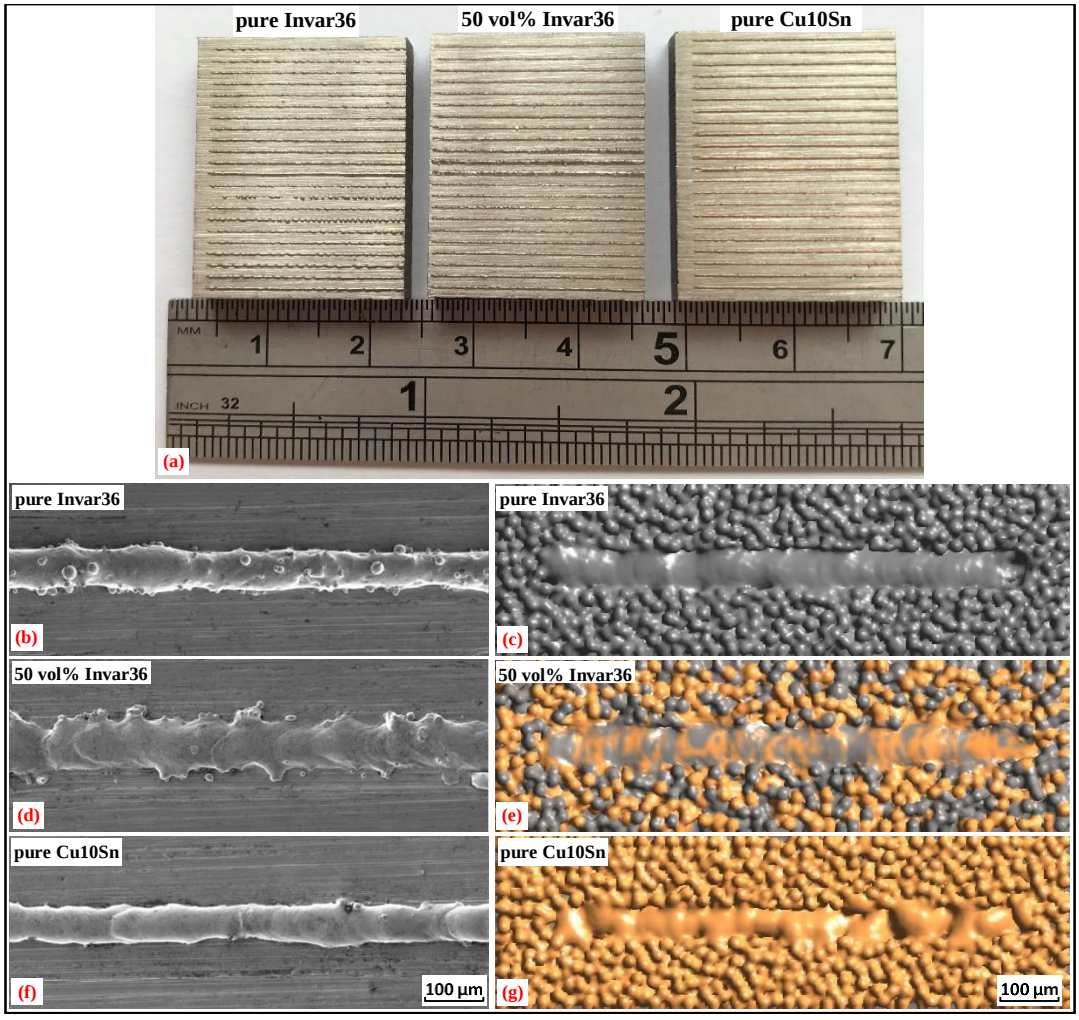

Fig. 2. Comparison of single-track morphology processed with different powder mixtures

The same process parameters were used during the numerical modelling, and the simulated single-track morphology of different powder mixtures were presented in Fig. 2(c), (e) and (g) for pure Invar36, 50 vol% Invar36, and pure Cu10Sn, respectively. The track width of each case was measured at ten different locations for both experimental and simulated results, and an average value was taken. The comparison of the averaged track width was shown in Table 3. The relative error was obtained between 6.32% and 8.60%, indicating that a good agreement was achieved between the experimental and simulated results, and hence validating the model.

Table 3. Comparison of the experimental and simulated average track width

Powder mixture content	Experimental (μm)	Simulated (μm)	Relative error (%)
pure Invar36	64.53	60.45	6.32
50 vol% Invar36	79.68	74.70	6.26
pure Cu10Sn	57.70	52.74	8.60

3.2 Effect of laser power

To investigate the effects of process parameters and powder mixture contents on the formation of defects in multi-material LPBF numerically, parameters including laser power, powder layer thickness and hatch spacing were varied, with the powder mixture initialised with different Invar36 contents. The laser scanning speed was kept constant at 150 mm/s and the laser beam diameter was applied as 80 μm. A scanning length of 800 μm was set for each scanning track with 5.3 ms heat duration.

The effect of laser power on the molten pool dynamics and track morphology with different material contents was firstly investigated. The powder bed was initialised with 40 μm layer thickness for three powder mixtures: pure Invar36, 75 vol% Invar36 + 25 vol% Cu10Sn and 25 vol% Invar36 + 75 vol% Cu10Sn. 125 W and 250 W laser powers were adopted in the single-track simulation. After the laser scanning, the morphologies of the powder bed are illustrated in Fig. 3 for different material compositions and laser powers.

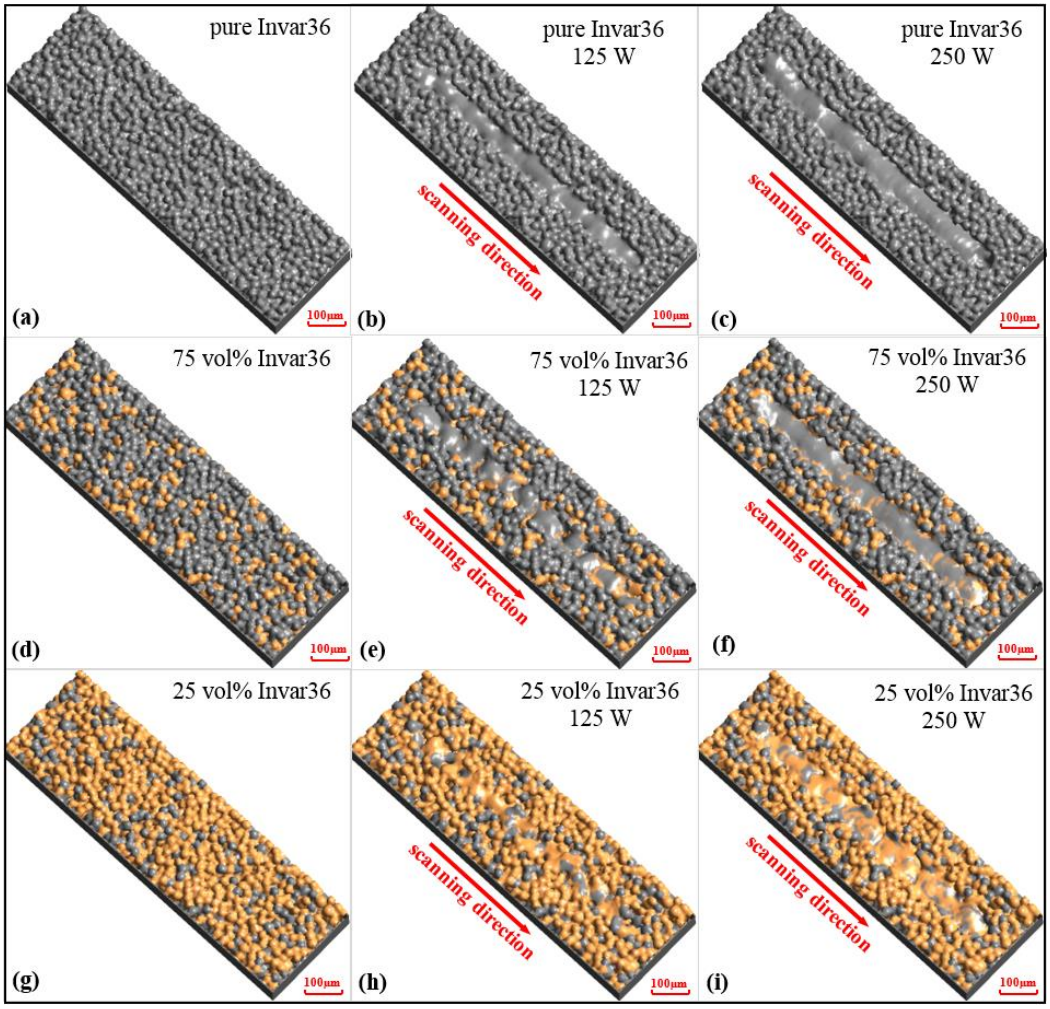

Fig. 3. Simulated morphology of powder bed before and after scanning with different material compositions and laser powers

It can be observed from Fig. 3(a) and (b) that smooth tracks were formed for pure Invar36 powder bed when applying both 125 W and 250 W laser powers. For the case of 75 vol% Invar36, a discontinuous track was formed on the scanning path with 125 W laser power as presented in Fig. 3(c), even though the applied laser power was the same as in Fig. 3(a). After increasing the laser power to 250 W, a continuous track was obtained for this material composition as presented in Fig. 3(d). Comparatively, a discontinuous track was also developed for 25 vol% Invar36 when applying 125 W, shown in Fig. 3(e), and with an increased laser power of 250 W, a smooth track was obtained for 25 vol% Invar36, as presented in Fig. 3(f).

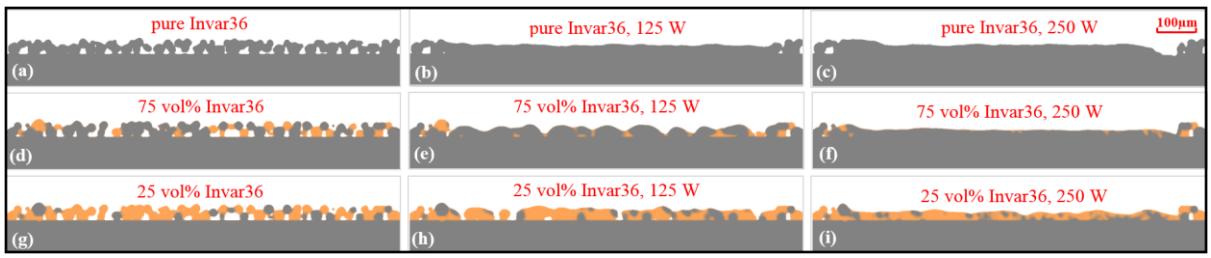

Fig. 4. Cross-section of the powder bed before and after laser scanning with different material compositions and laser powers

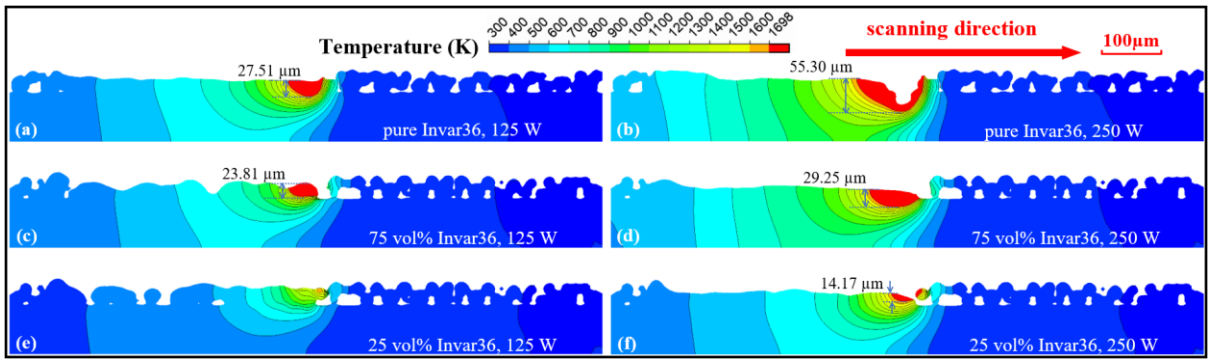

Fig. 5. Temperature distribution of the powder bed towards the middle of the scanning with different material compositions and laser powers

To compare the morphology of the scanned track more clearly, Fig. 4 shows the cross-section along the laser scanning path for all of the cases. A region of depression can be observed when approaching the end of the track for pure Invar36, seen in Fig. 4(c), when applying 250 W laser power, which could be related to keyhole formation. When applying 125 W laser power, discontinuous tracks were obtained in Fig. 4(e) and (h) for both the 75 and 25 vol% Invar36 cases. However, some differences are noticeable between the morphologies of these two tracks. In Fig. 4(e) some irregular shaped Cu10Sn phases were found in the discontinuously solidified Invar36 phase, which appear as balling defects, while in Fig. 4(h) some spherical and semi-spherical shaped Invar36 phases were observed embedded in the more continuously formed Cu10Sn track, which appear in the form of isolated clusters. After increasing the laser power to 250 W, tracks with smooth surfaces were obtained for 75 and 25 vol% Invar36 compositions, as shown in Fig. 4(f) and (i).

To better understand the temperature distribution and molten pool development for these different cases, temperature contours on the cross-section of the scanning path were plotted in Fig. 5. Temperatures greater than the liquidus point of Invar36 (1698 K) are shown in red to help display the profile of the molten pool shape for Invar36. The depth of molten pool was measured as the distance between the liquidus line at the molten pool bottom and the free surface. For pure Invar36 when applied with 125 W laser power, a continuous molten pool with 27.51 μm depth was obtained, as presented in Fig. 5(a). With an increased laser power of 250 W, higher temperature field was achieved, and a region of depression was formed in the molten pool front, as shown in Fig. 5(b). This was caused by the formation of keyholes, when the recoil pressure, created by the rapid material vaporization, exerts extremely high forces normal to the molten pool free surface [59]. Consequently, the molten pool depth increased dramatically to 55.30 μm. With a decreased Invar36 composition to 75 vol% when applying 125 W laser power, a discontinuous track was obtained, and the molten pool depth decreased to 23.81 μm, as presented in Fig. 5(c). The balling effect appeared due to the poor wetting characteristics of the liquid material without sufficient heat input [60], which indicates that 125 W was not sufficient to maintain a stable molten pool. After applying an increased laser power of 250 W, the balling effect disappeared and a continuous molten pool was developed with 29.25 μm molten pool depth, seen in Fig. 5(d). With a further decreased Invar36 composition to 25 vol% using 125 W laser power, isolated clusters were developed on the laser scanning path and the melting point of Invar36 was not reached at this moment, as presented in Fig. 5(e). A continuous track was formed after the laser power was increased to 250 W, although only a limited number of powder particles reached 1698 K with the molten pool depth of 14.17 μm for Invar36 powder, as shown in Fig. 5(f).

The comparison of Fig. 5(a), (c) and (e) reveals that with an increase in Cu10Sn composition from 0% to 75%, the molten pool depth of Invar36 decreased rapidly from 27.51 to 0 μm, despite having the same laser power applied. This was due to the fact that the laser absorptivity

of Cu10Sn powder is much lower compared with Invar36, while the thermal conductivity of Cu10Sn is higher than that of Invar36. As a result, the laser absorptivity of the mixed powder bed will decrease when increasing the Cu10Sn composition, and hence less energy will be absorbed by the powder bed. In addition, heat can be dissipated more quickly to the surrounding powder, as a result of the high thermal conductivity of Cu10Sn, making it more difficult for the Invar36 to reach the melting point. These two combined factors contributed to the decrease of the molten pool depth with an increased Cu10Sn content.

3.3 Effect of layer thickness

As can be concluded from the discussion above that the laser power has a significant impact on the morphology of the scanned track, and that different types of defects appear in different material compositions, even though the same laser power is applied. To investigate the formation of inter-layer defects, a second powder layer of 40 μm thickness was deposited on the first scanned track with different material compositions. The increased temperature due to the first scanned layer was applied to initialise the temperature distribution of the substrate and powder bed, in order to simulate the heat accumulation effect. This was achieved by exporting the temperature data of every powder element as well as the substrate at the last time-step of the first scanning layer. After the second powder layer was deposited on the powder bed, the temperature data was imported back to initialise the temperature profile of the calculation domain. After processing with different laser powers (125 W and 250 W), the morphologies of the second scanned layer with different material compositions are presented in Fig. 6.

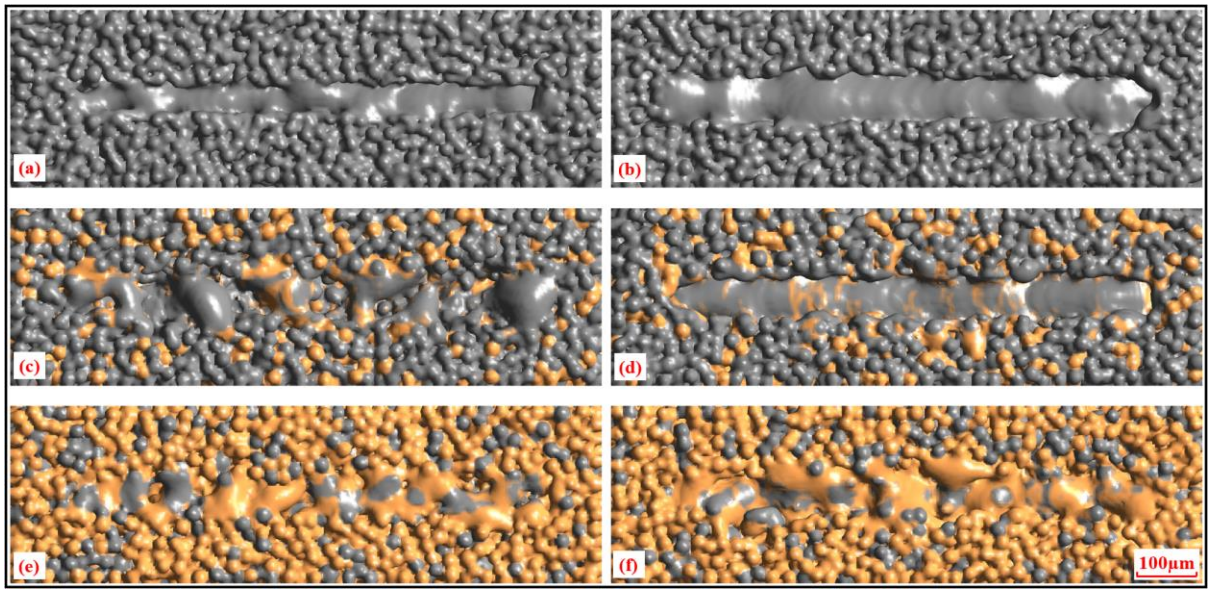

Fig. 6. Track morphology of the second scanned layer with 40 µm layer thickness: (a) pure Invar36 with 125 W, (b) pure Invar36 with 250 W, (c) 75 vol% Invar36 with 125 W, (d) 75 vol% Invar36 with 250 W, (e) 25 vol% Invar36 with 125 W, (f) 25 vol% Invar36 with 250 W

In a similar way to the first scanned track on the first layer, it can be observed that continuous tracks were formed for pure Invar36 when applying 125 W and 250 W laser powers as presented in Fig. 6(a) and (b). However, for the case with 125 W laser power, some surface unevenness can be noticed on the track surface, as illustrated in Fig. 6(a). Despite having the accumulated heat from the previously processed layer, a discontinuous track was obtained for 75 vol% Invar36 using 125 W (Fig. 6(c)). With an increased laser power of 250 W, a continuous track was formed, seen in Fig. 6(d). Isolated clusters were developed on the track surface for 25 vol% Invar36 when using 125 W (Fig. 6(e)), while a continuous track with some surface irregularity was obtained with an increased laser power of 250 W, as illustrated in Fig. 6(f). Fig. 7 demonstrates the cross-sections of the second scanned layer with different material compositions. When applying 125 W laser power, discontinuous tracks were obtained for both 75 and 25 vol% Invar36 cases, and defects, including balling effect, lack of fusion, and inter-layer pores, were formed as presented in Fig. 7(c) and (e). Attributed to the low laser absorptivity and high thermal conductivity of the Cu10Sn powder, the applied laser power was

not sufficient to maintain a good wetting behaviour between the molten powder and the previous scanned layer, which caused the appearance of balling defects, lack of fusion and irregular shaped inter-layer pores. Apart from the defects mentioned above, some spherical and semi-spherical shaped Invar36 powder particles were found embedded in the Cu10Sn phase seen in Fig. 7(e). To examine the mechanisms that cause these spherical and semi-spherical shaped Invar36 phases to form, molten pool development at six different moments for the case of 25 vol% Invar36 with 125 W laser power was analysed, and is demonstrated in Fig. 8. Two colour mappings were employed to differentiate the liquid fractions for Invar36 and Cu10Sn.

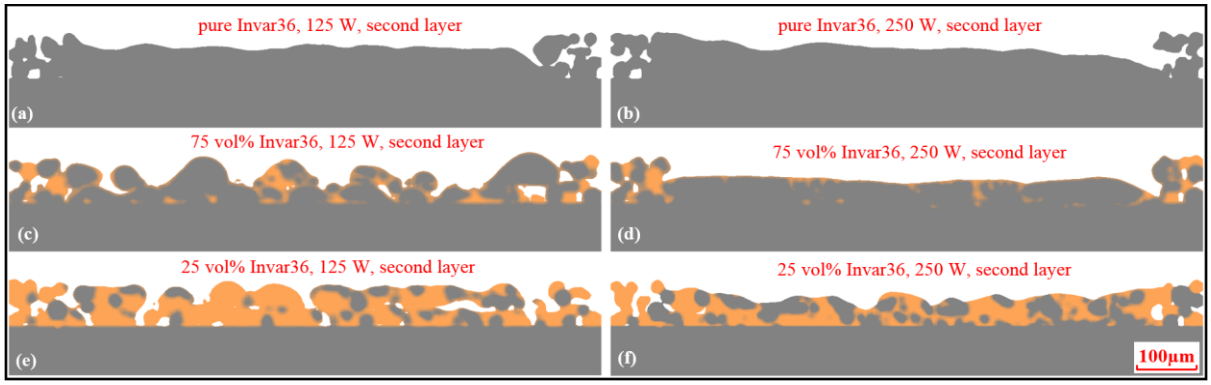

Fig. 7. Cross-sections of the second scanned layer with different material compositions and laser powers (40 μm layer thickness)

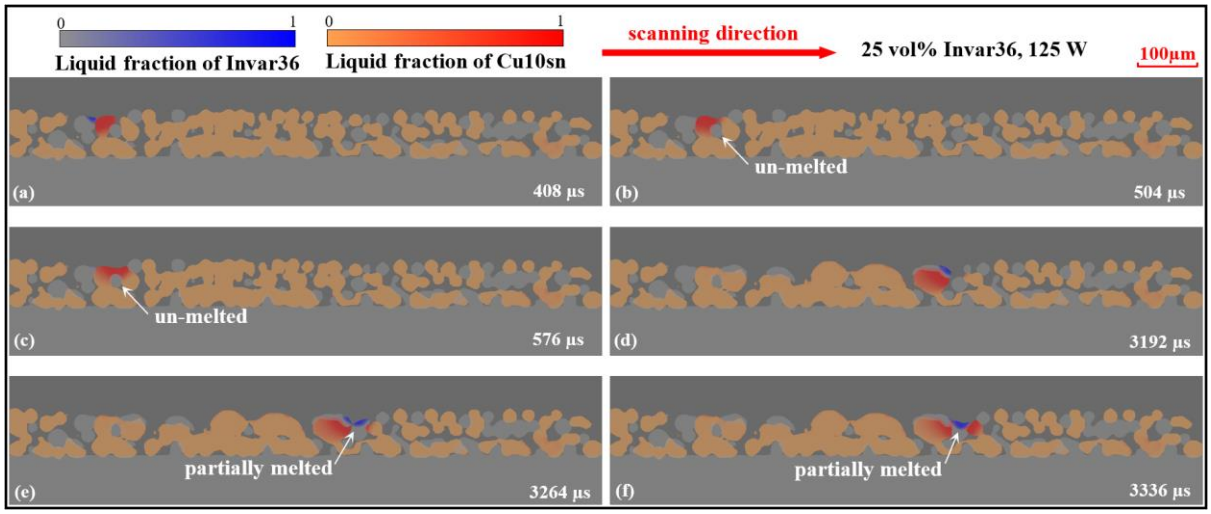

Fig. 8. Molten pool development of second scanned layer with 25 vol% Invar36 and 125 W laser power at six different moments (40 μm thickness)

As shown in Fig. 8(a), the Cu10Sn powder which was exposed directly to the laser beam melted first, reaching its melting point at 408 µs. Due to the surface tension force [61], the individual molten Cu10Sn powder had the potential to form a larger molten droplet with surrounding molten powder to reduce the overall surface area, as presented in Fig. 8(b). For the Invar36 powder particles deposited at the lower level of the powder bed, which were not directly exposed to the laser beam, the heat conducted from the surrounding Cu10Sn powder did not provide enough energy to reach the melting point of Invar36 when the applied laser power was low. Consequently, these Invar36 powder particles remained un-melted and became embedded in the melted Cu10Sn powder, as illustrated in Fig. 8(b) and (c). For those Invar36 powder particles that could be directly impacted by the laser beam, they started to melt after reaching the melting point and fused with the nearby molten powder. However, the heat was dissipated quickly, attributed to the high thermal conductively of the surrounding Cu10Sn powder, and without enough heat input only a small portion of the Invar36 powder could be melted, as presented in Fig. 8(d-f). After solidification, these partially melted Invar36 powder particles were embedded in the melted Cu10Sn powder. Although only limited number of the powder particles on the scanning path reached the melting point of Invar36, most of the Cu10Sn powder particles were still melted as a result of the low melting point of Cu10Sn.

It can be concluded from the above discussion that despite having the accumulated heat from the previously processed layer, discontinuous tracks were obtained for 75 and 25 vol% Invar36 cases when using 125 W laser power. To examine the impact of layer thickness on the defect formation, a second powder layer with an increased thickness of 50 µm was deposited in the other four cases, and the cross-sections of the track morphology after laser scanning is presented in Fig. 9. Continuous tracks were formed for pure Invar36 and 75 vol% Invar36 using 250 W laser power and 50 µm layer thickness as seen in Fig. 9(b) and (c). In contrast, discontinuous tracks with defects, including balling effect, lack of fusion and inter-layer pores, were developed for the cases of pure Invar36 with 125 W and 25 vol% Invar 36 with 250 W,

as demonstrated in Fig. 9(a) and (d) respectively. One should note that with 40 µm layer thickness some surface unevenness was already observed for these two cases, despite having no defects, as presented in Fig. 6(a) and (f). After increasing the powder layer thickness from 40 to 50 µm, defects started to occur for these two cases.

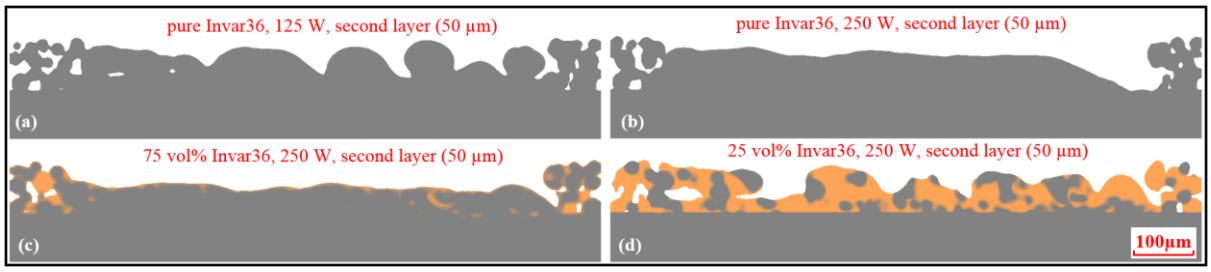

Fig. 9. Cross-sections of the second scanned layer with different material compositions and laser powers (50 µm layer thickness)

Fig. 10 compares the temperature distribution between the second scanning layer applied with 40 and 50 µm layer thicknesses for 25 vol% Invar36, with 250 W laser power, at the same moment during the scanning process. Two colour mappings were employed to differentiate the molten pool profile for Invar36 and Cu10Sn. A good wetting behaviour between the molten powder and the previous scanned layer was achieved in Fig. 10(a) and (b) for the case of 40 µm layer thickness, which contributed to a continuous track morphology. With an increased layer thickness of 50 µm, the molten pool region of Cu10Sn also increased seen in Fig. 10(b) and (d). The reduced region of temperature greater than the melting point of Invar36 shown in Fig. 10(c) could be related to the variation of Invar36 distribution on the powder bed. Considering that 75 vol% of the powder was Cu10Sn in this case, the overall molten pool size increased. With an increased powder layer thickness, apart from introducing more powder to the powder bed, more air between individual powder particles was also introduced. Consequently, the effective thermal conductivity of the powder bed decreased, as a result of the low thermal conductivity of air [62], and heat could not, therefore, be dissipated quickly to the previous layer as well as the substrate underneath. Therefore, a higher molten pool volume

would be developed with a larger powder layer thickness. Molten powder particles have the potential to form a bigger droplet with surrounding molten powder if a connected liquid channel with the previous layer could not be developed, as shown in Fig. 10(d). Therefore, a continuous molten pool would fail to form when applying a higher layer thickness while using the same laser power, which contributed to the formation of various types of defects after solidification. This is consistent with the previous research from Cao [63], which stated that to achieve a continuous track when using a large layer thickness, a higher powder bed tightness as well as higher heat input should be adopted in order to ensure a decent fusion with the previous processed layer, and hence preventing the formation of defects.

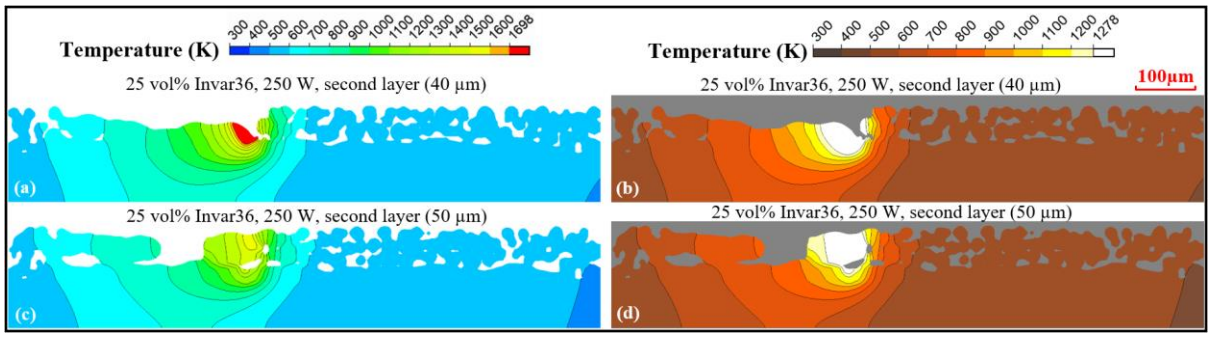

Fig. 10. Comparison of temperature distribution between the second scanning layer applied with 40 and 50 μm layer thicknesses (25 vol% Invar36 and 250 W laser power)

A comparative investigation was conducted by increasing the thickness of the second layer to 60 μm for pure Invar36 and 75 vol% Invar36 with 250 W laser power, and the resultant morphologies of the scanned tracks are shown in Fig. 11. With an increased layer thickness from 50 to 60 μm, although continuous tracks were still obtained, some surface unevenness started to appear, giving an early indication that the applied energy could no longer maintain a stable molten pool under such powder layer thickness.

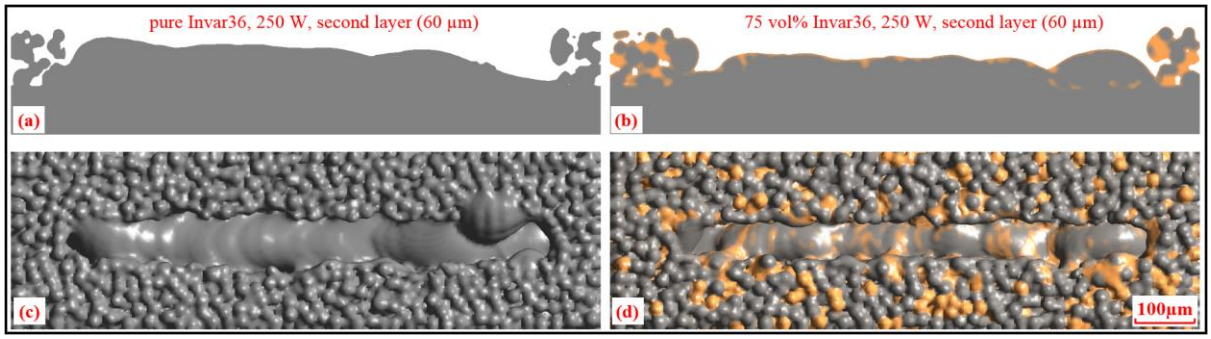

Fig. 11. Crossing section and track morphology of the second scanned layer with 60 µm layer thickness: (a) and (c) pure Invar36, (b) and (d) 75 vol% Invar36

3.4 Effect of hatch spacing

To investigate the formation of inter-track defects, a second scanning track was simulated for cases using 125 W laser power, with a hatch spacing of 60 µm. The increased temperature due to the first scanned track was applied to initialise the temperature distribution of the substrate and powder before conducting the second track, in order to simulate the effect of heat accumulation. After processing with different material contents, the morphologies of the first and second scanned track are presented in Fig. 12. As discussed above, when using 125 W laser power, discontinuous tracks were obtained for 75 vol% and 25 vol% Invar36 during the first scanning track, as shown in Fig. 12(c) and (e). After scanning with 60 µm hatch spacing, discontinuous tracks were again obtained for these two cases, as presented in Fig. 12(d) and (f), indicating that a continuous molten pool could not be developed despite having the heat accumulated from the previous scanned track. As for the case of pure Invar36, although the first scanned track was continuous (Fig. 12(a)), some partially melted powder particles can be seen on the interface of the two scanned tracks, as illustrated in Fig. 12(b).

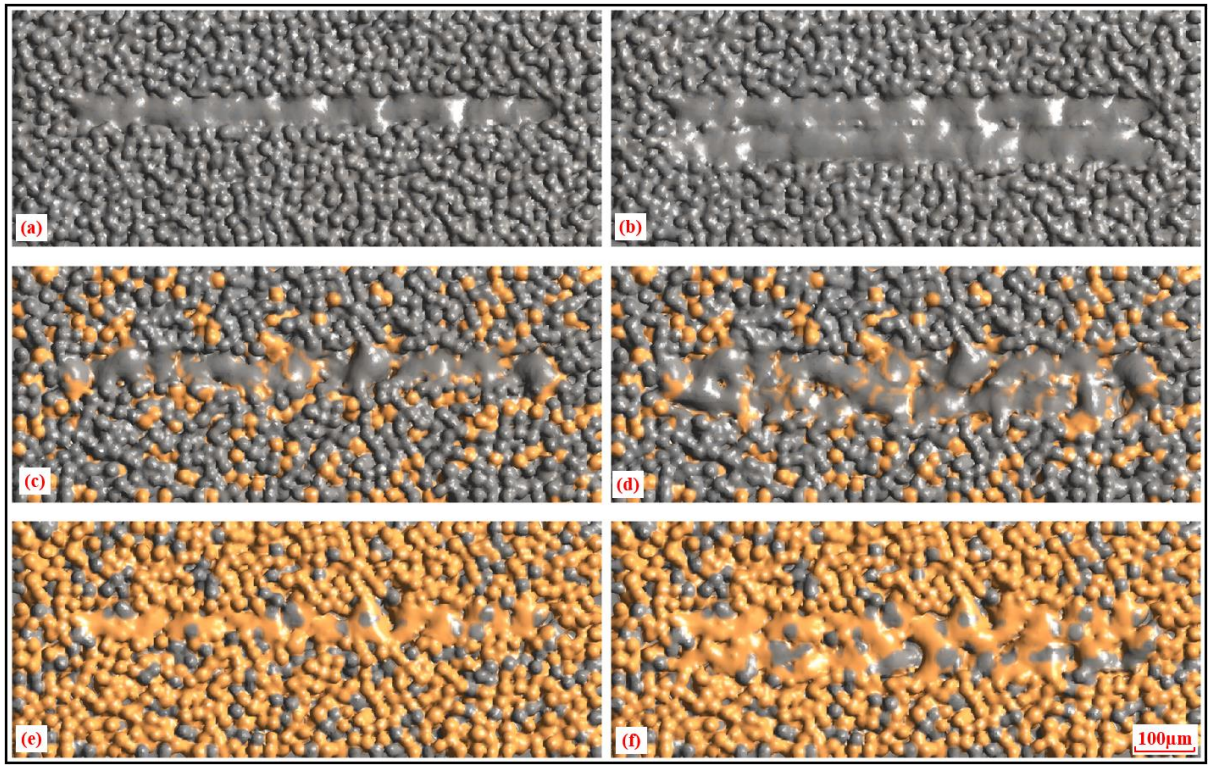

Fig. 12. Track morphologies of different material compositions with 125 W laser power and 60 μm hatch spacing: (a-b) pure Invar36 first and second track, (c-d) 75 vol% Invar36 first and second track, (e-f) 25 vol% Invar36 first and second track

To better understand the forming mechanisms of inter-track defects, and to evaluate the impact of hatch spacing, a second scanning track with 250 W was simulated, using different hatch spacings of 60 μm, 80 μm and 100 μm and different material compositions. The resultant morphologies of the scanned track are presented in Fig. 13, Fig. 14 and Fig. 15 for the case of pure Invar36, 75 vol% Invar36, and 25 vol% Invar36, respectively. Smooth tracks were obtained for all material compositions when applying 60 μm hatch spacing, seen in Fig. 13(b), Fig. 14(b) and Fig. 15(b). With an increased hatch spacing of 80 μm, some partially melted Invar36 powder particles started to appear between two adjacent tracks on the interface of the molten pool, as presented in Fig. 13(c), Fig. 14(c) and Fig. 15(c). When further increasing the hatch spacing to 100 μm, more partially melted Invar36 powder particles mixed with un-melted Invar36 powder were observed for the pure Invar36 and 75 vol% Invar36 cases, as shown in Fig. 13(d) and Fig. 14(d). With the mixed powder content of 25 vol% Invar36, in addition to

Invar36 powder which could not be fully melted, some partially melted and un-melted Cu10Sn powder was also noticed on the boundary of the two scanned tracks, as presented in Fig. 15(d).

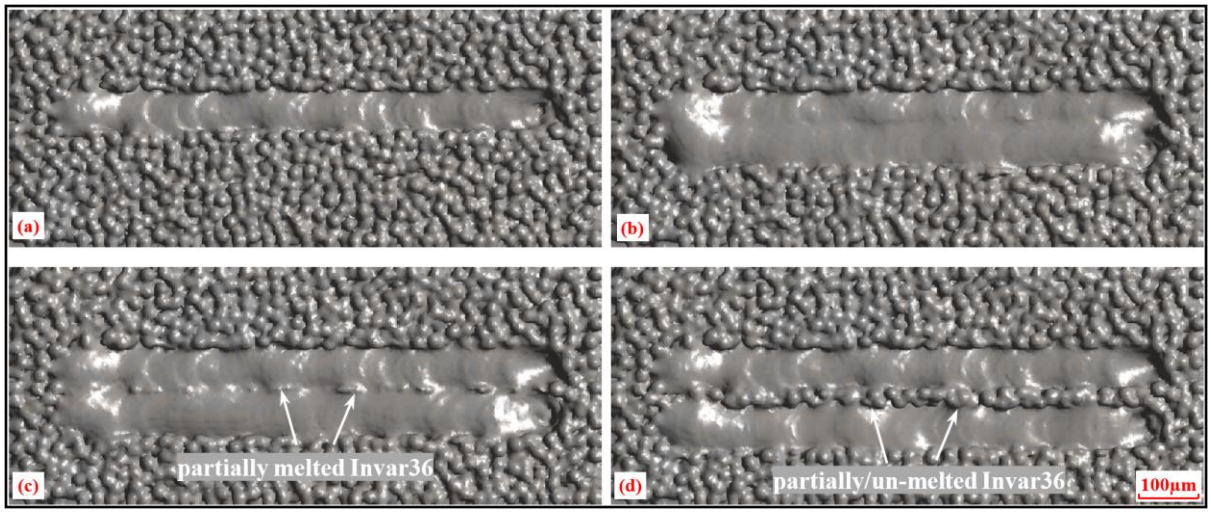

Fig. 13. Track morphology of pure Invar36 with 250 W laser power: (a) first track, (b) 60 μm hatch spacing, (c) 80 μm hatch spacing and (d) 100 μm hatch spacing

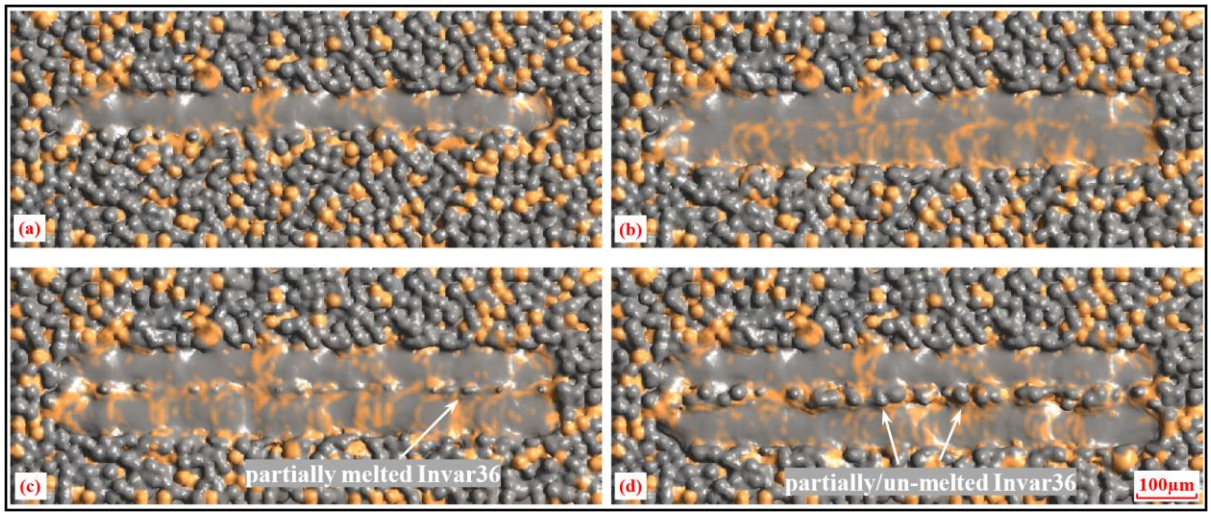

Fig. 14. Track morphology of 75 vol% Invar36 with 250 W laser power: (a) first track, (b) 60 μm hatch spacing, (c) 80 μm hatch spacing and (d) 100 μm hatch spacing

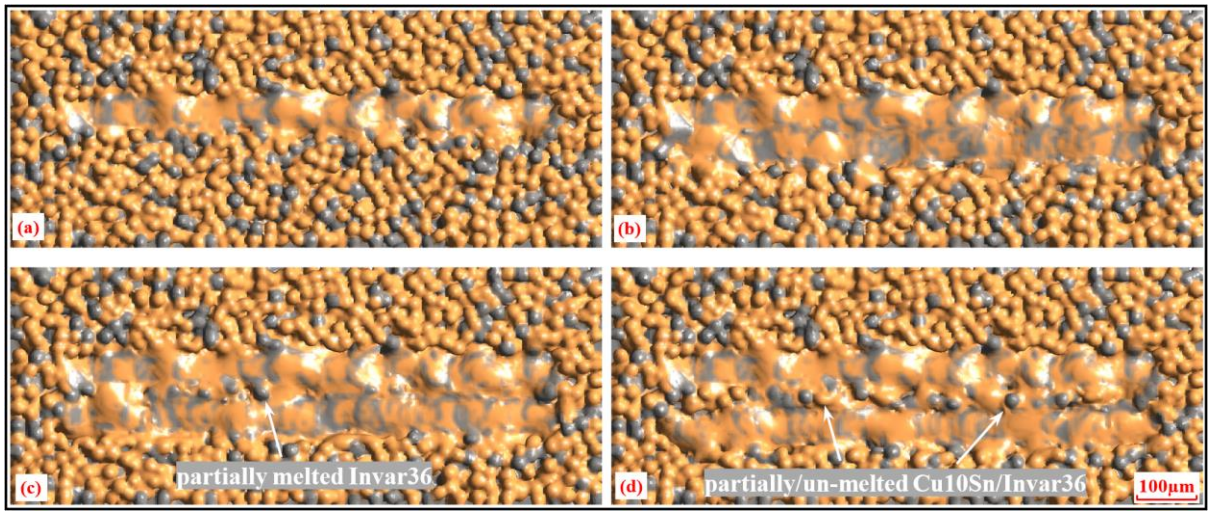

Fig. 15. Track morphology of 25 vol% Invar36 with 250 W laser power: (a) first track, (b) 60 μm hatch spacing, (c) 80 μm hatch spacing and (d) 100 μm hatch spacing

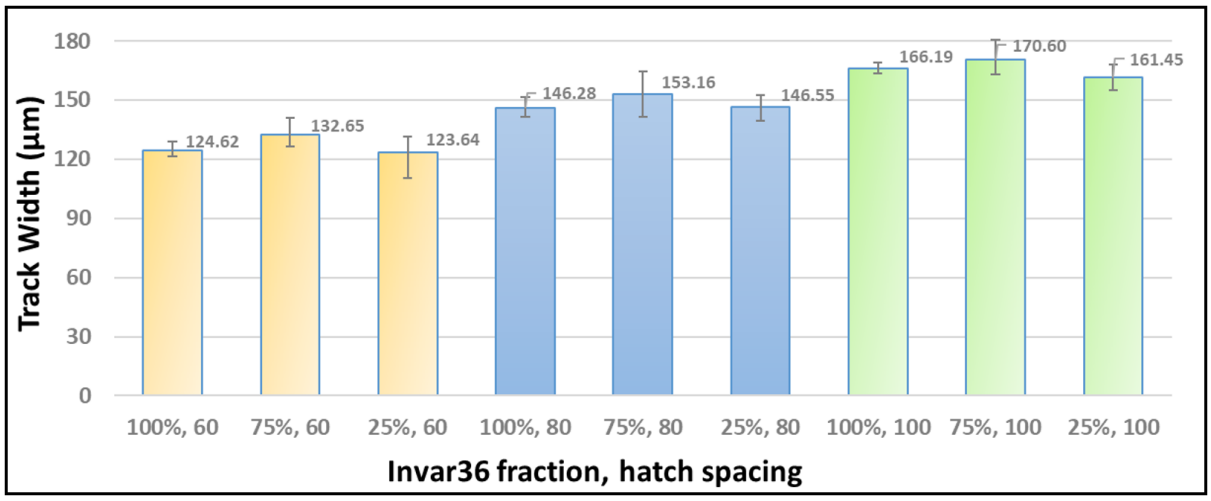

Fig. 16. Comparison of track width with different material compositions and hatch spacings

Fig. 16 shows the comparison of the track widths achieved when processing different material compositions, where the different colours represent cases with different hatch spacings. The track width was measured between the outer solidified edges of the two tracks and averaged over ten measurements. For the cases with 60 μm hatch spacing (coloured in yellow), it can be seen that the track width increased from 124.62 μm to 132.65 μm when decreasing the Invar36 content from 100 to 75 vol%. With a further decreased Invar36 content to 25 vol%, the track width decreased to 123.64 μm. This trend was also shared with the other hatch spacing groups,

where the largest track width was always obtained when the Invar36 content was 75 vol%. Additionally, the deviation of the track width was found the smallest for pure Invar36 in each hatch spacing group. This phenomenon was also reported by Sun et al. [31], who found that in a IN718/Cu10Sn multi-material LPBF system the track width would first increase and then decrease when reducing the IN718 content from 100 to 0 vol%, and the least track width fluctuation was found for cases with pure IN718.

To understand these phenomena, Fig. 17 shows the development history of the molten pool volume of the two scanning tracks with different material compositions and hatch spacings. As can be observed from Fig. 17(a) that the molten pool volume for pure Invar36 increased rapidly at the beginning of the first scanning track before reaching a stable state at around 450 μs. There is a big drop in the molten pool volume at 5.3 ms when the second scanning track started. Since the beginning of the second scanning track was at the same starting point as the first track, the local temperature had already decreased through heat dissipation to surrounding powder and to atmosphere, which led to the decrease in the volume of molten pool when starting the second track. However, as a result of the heat accumulation effect, the maximum molten pool volume was higher in the second scanning track compared with the first track. One interesting finding is that, despite the different hatch spacings investigated, no distinct variance in molten pool volume with hatch spacing is observed among cases with pure Invar36 (Fig. 17(a)). As for the cases with 25 vol% Invar36, shown in Fig. 17(c), comparable molten pool development histories were also obtained with different hatch spacings applied. For cases with 75 vol% Invar36, as illustrated in Fig. 17(b), similar histories of molten pool volume were developed for tracks with 60 μm and 80 μm hatch spacings. Unlike the other material composition groups, a much higher maximum molten pool volume was obtained when the hatch spacing was applied as 100 μm, and it took the longest for it to reach the maximum. This could be attributed to powder close to the molten pool being melted and dragged towards the liquid metal, due to the surface tension force, to form the track [64]. When a small hatch spacing

is used, only a limited number of powder close to the scanning path would have been melted to obtain an increased track width. As a result, the molten pool volume would have mostly formed from the re-melting of the previous track. After increasing the hatch spacing, combined with distinct differences in the thermal properties of the two powder materials, more Cu10Sn powder would be melted in the case with 100 µm hatch spacing, which has contributed to a dramatic increase in the molten pool volume.

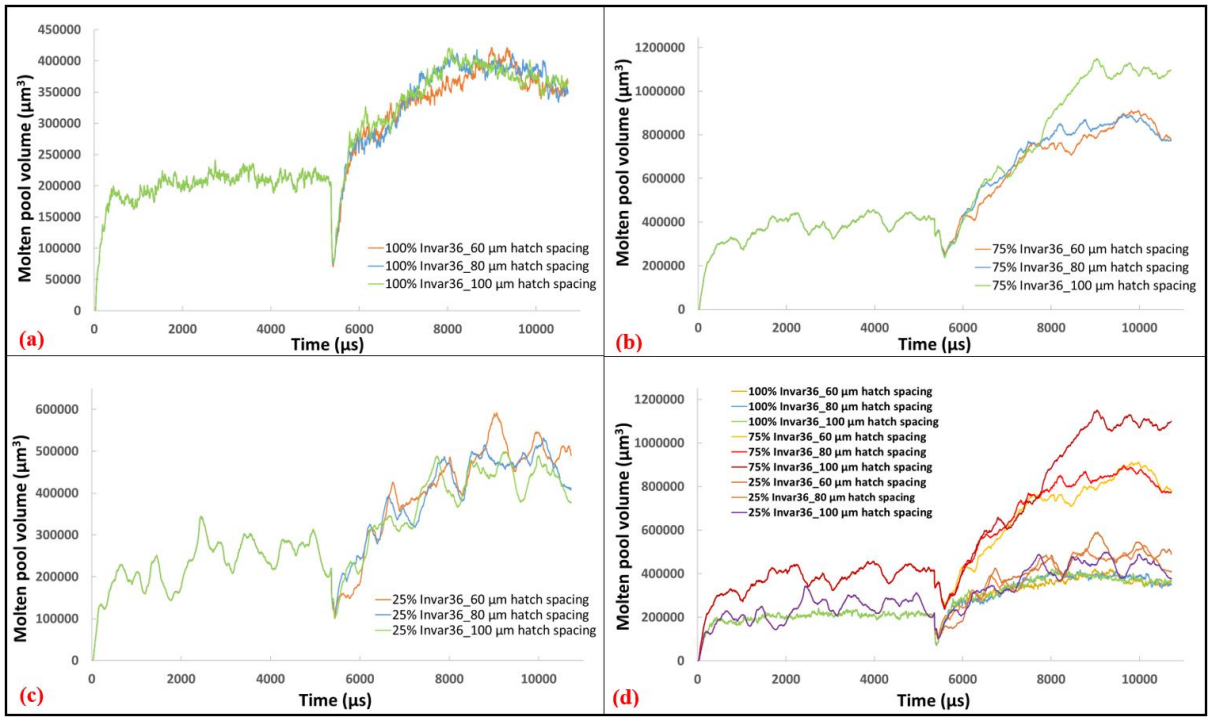

Fig. 17. Molten pool development history of two tracks with different material compositions and hatch spacings: (a) pure Invar36, (b) 75 vol% Invar36, (c) 25 vol% Invar36, (d) comparison of all cases

Fig. 17(d) shows a comparison of the molten pool development history of all cases with different hatch spacings and material compositions. It is evident that the 75 vol% Invar36 cases have the highest molten pool volume during both the first and second scanning tracks. This could explain why the track width obtained was the largest for cases with 75 vol% Invar36, as shown in Fig. 16. The pure and 25 vol% Invar36 cases have similar molten pool volume which is consistent with the similar track width of these two material composition groups. It can also

be noted from Fig. 17(d) that the least fluctuation in the molten pool evolvement was found in cases with pure Invar36. This can be attributed to the fact that variations in the local composition of the mixed powder, due to the randomly distributed Cu10Sn in the powder bed, could result in a fluctuation in the laser energy absorption along the scanning path. Combined with the distinct differences of the thermal properties, this leads to more fluctuations in molten pool development when processing the powder bed with mixed materials, compared with a single material. This explains why the least deviations in the track width are observed in cases with pure Invar36 powder bed, as depicted in Fig. 16.

Fig. 18 illustrates the temperature distribution of the second track using 80 μm hatch spacing with different material compositions, where two colour mappings were adopted to present the molten pool profile for Invar36 and Cu10Sn. As discussed in the previous section, the temperature of the powder bed will decrease when reducing the Invar36 content while applying the same laser power, seen in Fig. 18 (a), (c) and (e). When presented with a different colour mapping with a lower maximum temperature, it can be seen that despite having a larger molten pool region for Cu10Sn (compared with Fig. 18 (a), (c) and (e)), the area with a temperature greater than the liquidus point of Cu10Sn (1278 K) still became smaller when decreasing the Invar36 content from 100 to 25 vol%, as presented in Fig. 18 (b), (d) and (f). However, due to the increase in Cu10Sn content, which has a much lower melting point and higher thermal conductivity, the total molten pool volume, as well as the track width, increased when decreasing the Invar36 content from 100 to 75 vol%. This indicates that the slight drop in laser absorption was compensated by the difference of the thermal properties introduced by the Cu10Sn powder at this powder mixture level. When further decreasing the Invar36 content to 25 vol%, the dramatic drop in laser absorption of the powder bed is no longer counterbalanced by the high thermal conductivity and low melting point of the Cu10Sn powder. Consequently, the molten pool volume and the track width decrease with a further decreased Invar36 content.

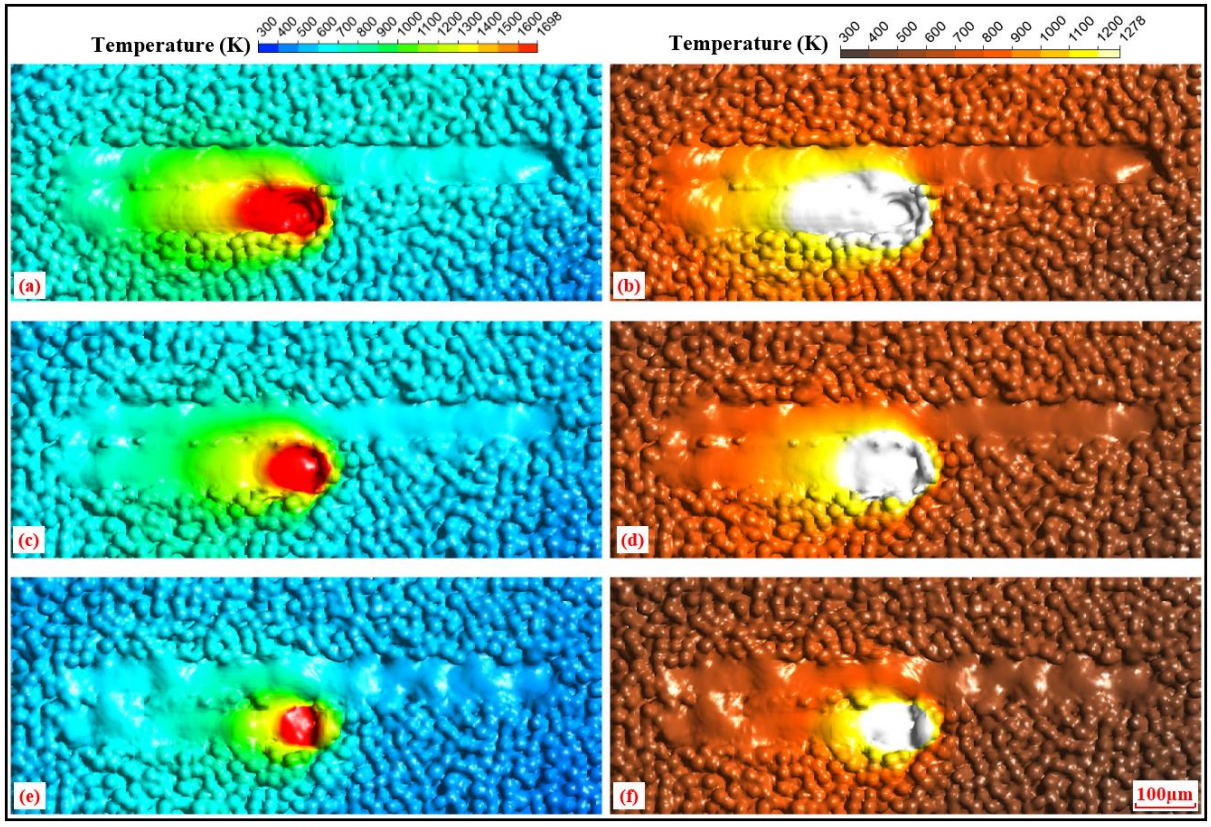

Fig. 18. Temperature distribution of the second scanning track with 80 μm hatch spacing presented in two colour mappings, (a, b): pure Invar36, (c, d): 75 vol% Invar36, (e, f): 25 vol% Invar36

3.5 Functional graded materials

It can be concluded from the above study that the process parameters and material contents serve pivotal roles in the defect formation, track morphology and molten pool dynamics in a multi-material LPBF system. In addition to studies of powder bed deposited with a fixed material composition, FGM structures fabricated with a compositional change of two materials have been reported in both horizontal [65] and vertical [26] building directions. This section discussed the FGM simulations conducted in horizontal and vertical directions.

3.5.1 FGM in horizontal direction

Fig. 19 shows a longer calculation domain with dimensions of 400 μm × 3000 μm × 140 μm. The powder bed was first initialised with pure Invar36 powder to establish a basis for

comparison with the FGM simulation. Process parameters of 500 W laser power and 800 mm/s scanning speed were employed to simulate a single track with 2800 µm scanning distance. Fig. 19(b)-(d) present the track morphology, temperature distribution and cross-section of the scanned track, respectively. As shown, a continuous track was obtained when scanning the pure Invar36 powder bed. The powder bed distribution for the simulation of FGM in horizontal direction is illustrated in Fig. 20(a), where the long calculation domain was evenly divided into five sections, with 600 µm length for each section. The FGM powder bed was generated by gradually increasing the deposition rate of Cu10Sn powder in each section from 0 to 100% (left to right), while conversely decreasing the deposition rate of Invar36 powder from 100 to 0%. The process parameters were first applied constantly along the scanning path and the resultant morphology and the temperature distribution were presented in Fig. 20(b)-(d). A discontinuous molten pool was obtained for Cu10Sn at the end of the scanning process, as presented in Fig. 20(c). In addition, defects, including balling effect and isolated clusters, were formed on the scanning track, seen in Fig. 20(b) and (d), indicating that the constant energy applied was not enough to maintain a continuous molten pool. In order to obtain a better wetting characteristic of the molten pool, and hence a continuous scanned track, laser power was increased from 500 W to 667 W, 833 W and 1000 W along the scanning at 624 µs, 2000 µs and 2400 µs, respectively. An enlarged molten pool and a smooth track surface were achieved, as illustrated in Fig. 21. One should note that a higher scanning speed was adopted in this simulation to reduce the calculation time, which required a higher applied laser power. In normal experimental conditions, due to the limitation of the available maximum laser power, lower scanning speed could be adopted combined with lower laser power.

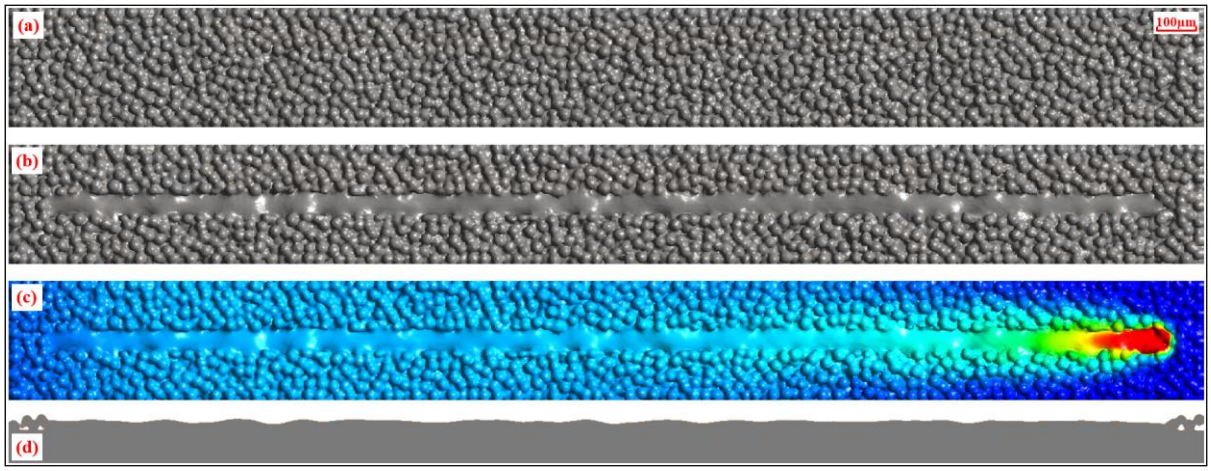

Fig. 19. Track formation and temperature distribution of pure Invar36 powder bed

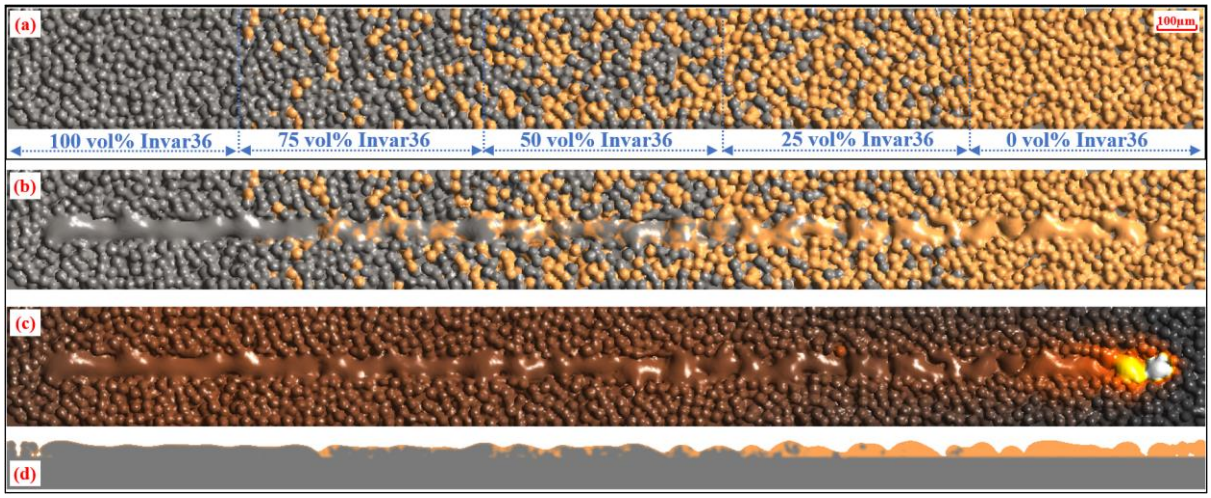

Fig. 20. Track formation and temperature distribution of FGM in horizontal direction scanned with constant laser power

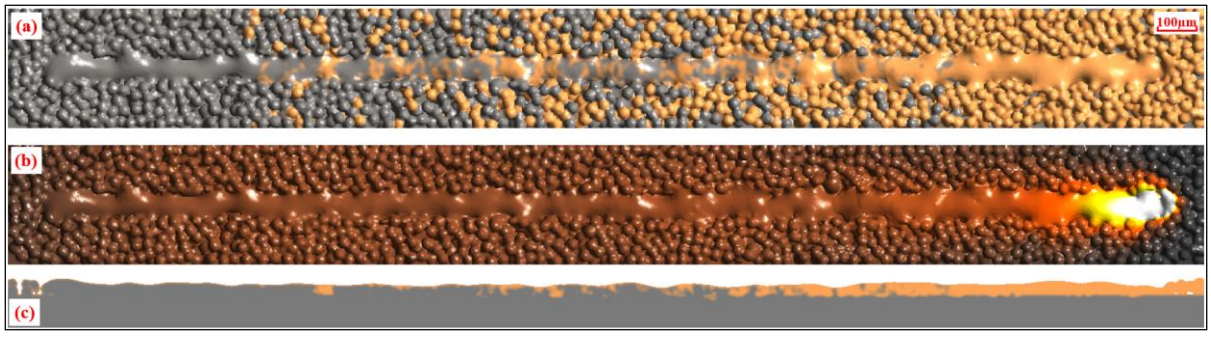

Fig. 21. Track formation and temperature distribution of FGM in horizontal direction scanned with optimised laser power

Fig. 22 compares the development history of the molten pool volume for the three cases. The molten pool volume for pure Invar36 stayed stable after reaching its maximum (blue line). For the FGM powder bed, although the same material composition was deposited in the first section compared with the pure Invar36 case, some differences still existed at the beginning of the scanning process, which could be related to randomly distributed powder on the powder bed. An increase in the molten pool volume could be noticed when the laser beam entered the 75 vol% Invar36 section, which was resulted from the higher thermal conductivity and lower melting point of Cu10Sn. The molten pool volume experienced a rapid decrease at around 2000 μs when the powder bed section with higher Cu10Sn content was scanned, indicating that the dramatic drop in laser absorption of the powder bed at this section could no longer be counterbalanced by the thermal properties of the Cu10Sn powder. Consequently, a discontinuous track with defects was formed. By applying an optimised laser power (black line), despite having some fluctuations along the scanning process (caused by the local composition of the powder mixture), a relatively stable molten pool volume was obtained, which contributed to a continuous scanned track for the FGM powder bed.

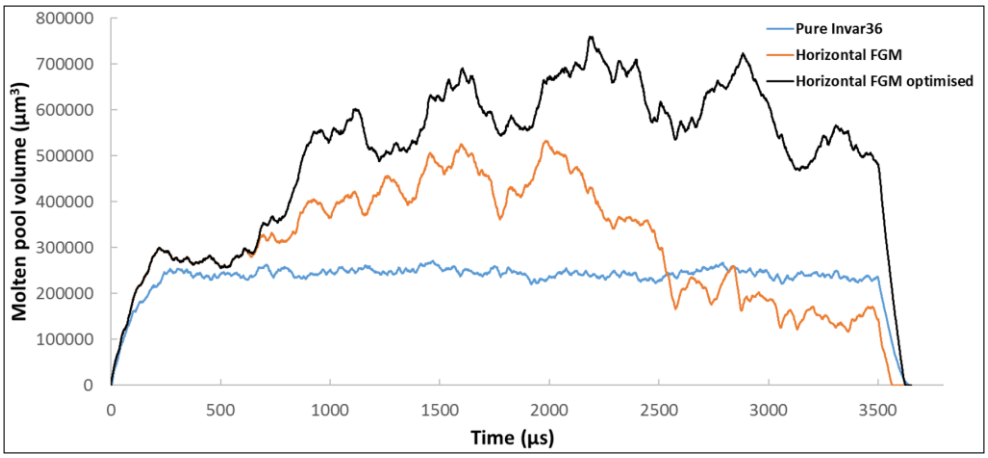

Fig. 22. Comparison of molten pool development history of FGM in horizontal direction

3.5.2 FGM in vertical direction

A simplified demonstration of FGM in vertical direction was presented in Fig. 23. Five layers were simulated, where the first layer was deposited with pure Invar36 powder and the Invar36 content was gradually decreased to 0 at the fifth layer which was deposited with pure Cu10Sn. An increased laser power was applied for each consecutive layer to compensate for the reduced laser absorption and hence to maintain a continuous scanning track. FGM in vertical direction of five layers was illustrated in Fig. 23(f). Since only one layer was processed for each material composition group, some Invar36 phase can be observed in the last scanning layer of pure Cu10Sn, which resulted from the convection flow inside the molten pool [30]. In real experimental conditions, multiple layers of each material composition would normally be processed to minimise the dilution and obtain an FGM component of large scale as well as smooth transitions between different compositions [66].

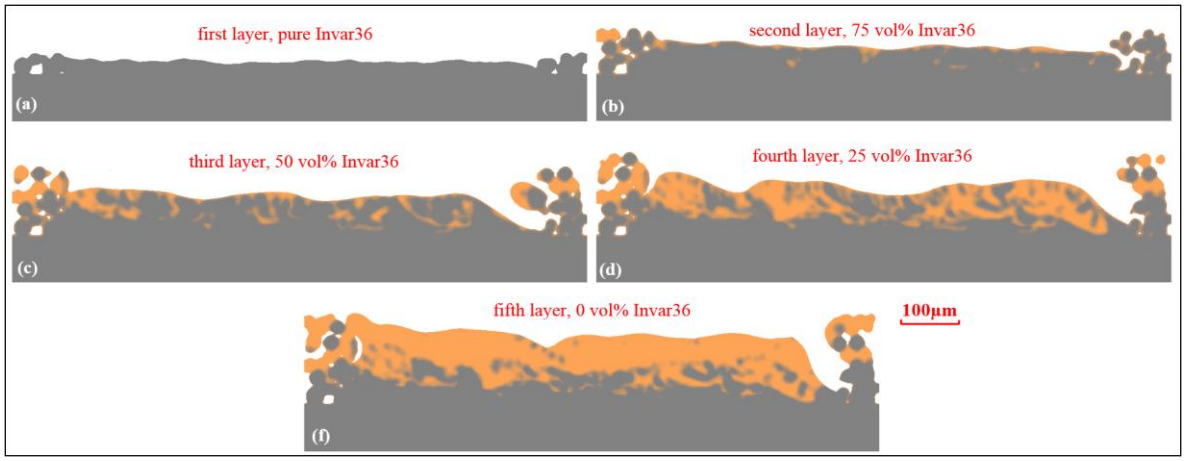

Fig. 23. Cross-section of the FGM in vertical direction of five layers

4. Experimental investigation

4.1 Experimental procedure

Square samples with dimensions of 8 × 8 × 4 mm were fabricated using different process parameters and material contents, and electric discharge machining (EDM) was utilised to slice

the samples into thin specimens of 1 mm thickness. After polishing and grinding, the samples were etched by the Marble's reagent (50 ml HCl, 10 g CuSO4, and 50 ml water) [67], which was suitable for nickel, Ni-Cu, and Ni-Fe alloy. A digital microscope (KEYENCE, VHX-5000) was employed to examine the macrostructure and microstructure of the sample cross-sections. An SEM (Zeiss Sigma VP FEG SEM) equipped with EDS mapping (Oxford Instruments X-maxN 150) was used to obtain a high-magnification observation of the microstructure and the element distributions of the specimens.

4.2 Results and discussion

Samples were fabricated with three material contents: pure Invar36, 75 vol% Invar36 + 25 vol% Cu10Sn and 25 vol% Invar36 + 75 vol% Cu10Sn. The process parameters, including laser power, scanning speed and hatching spacing, were varied to investigate the mechanisms by which the defects form. Laser volumetric energy density (VED) [3] was used to examine the combined impact of these process parameters; VED is defined as: $\mathrm{VED} = P/(t * v * h)$, where P is the laser power (W), t is the layer thickness (mm), v is the scanning speed (mm/s) and h is the hatch spacing (mm).

Fig. 24 presents the macrostructure and microstructure of different powder mixtures processed with the same VED of 208 J/mm^3 (P = 125 W, v = 150 mm/s, h = 100 μm and t = 40 μm). For pure Invar36, some spherical pores were noticed in some processing layers and fish-scale shaped molten pools were obtained without obvious interlayer defects, as shown in Fig. 24(a) and (b) respectively. The spherical pores could be related to the trapped gas phase as a result of the keyhole formation [32]. Despite using the same VED as compared with the pure Invar36 case, completely different cross-section morphologies were obtained when processing 75 vol% Invar36 + 25 vol% Cu10Sn, as presented in Fig. 24(c) and (d). Clear interfaces between two layers can be observed, and some un-melted, as well as un-fully melted powder particles, can be found in the lower level of the scanned layer.

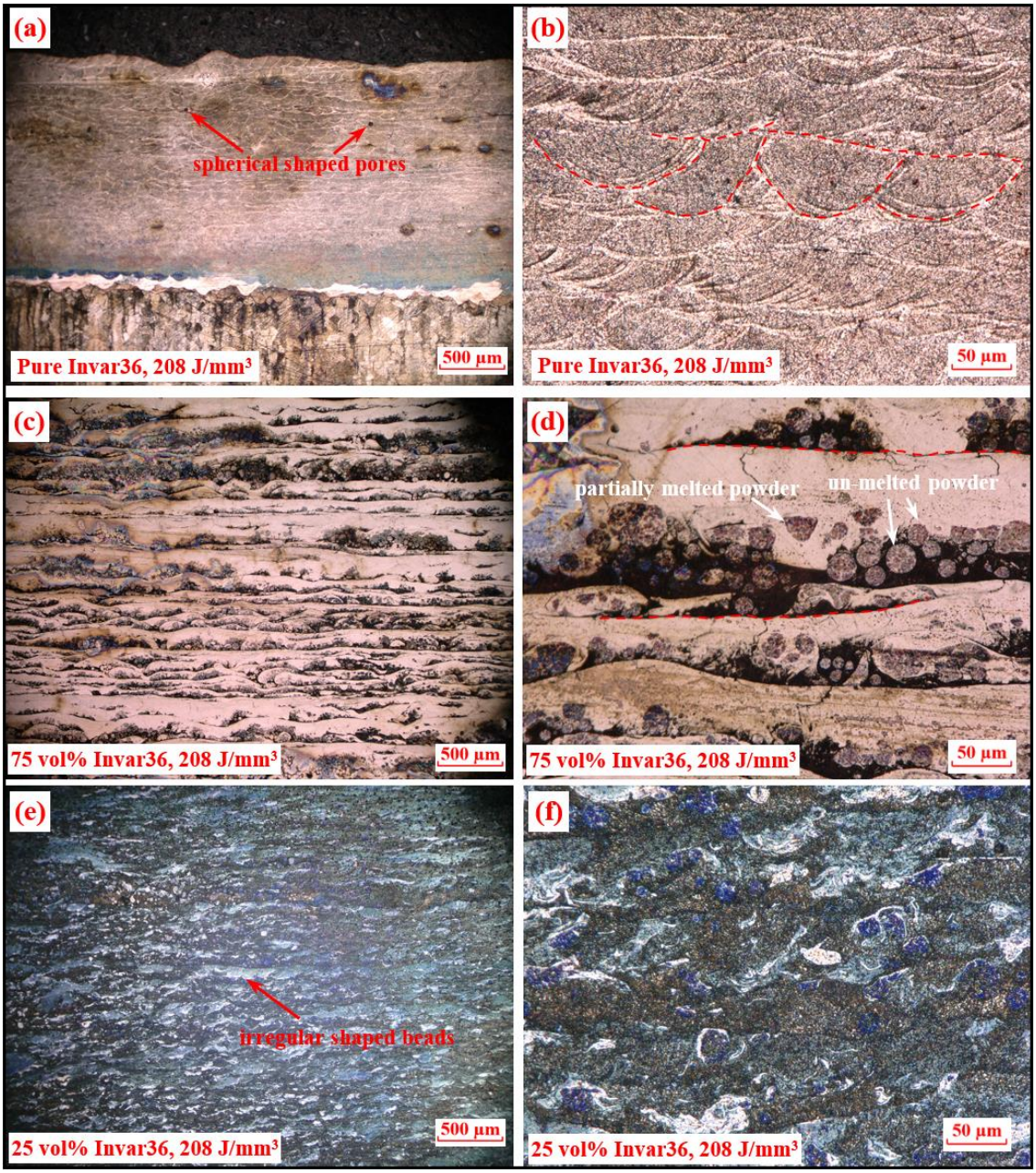

Fig. 24. Macrostructure and microstructure of different powder mixtures processed with 208 J/mm^3 VED: (a, b) pure Invar36, (c, d) 75 vol% Invar36 + 25 vol% Cu10Sn, (e,f) 25 vol% Invar36 + 75 vol% Cu10Sn

To reveal the material compositions of those un-melted and partially melted powder particles, EDS mapping was employed to examine the local element distribution, as shown in Fig. 25. It can be noticed that these un-melted and partially melted powder particles were all Invar36 (coloured in green), while the metal bonding the Invar36 phases was Cu10Sn (coloured in red). This validates the simulated results, suggesting that the laser energy applied was able to melt

all of the Cu10Sn powder, while leaving some of the Invar36 powder partially un-melted. The EDS mapping also depicts that the interfaces between the layers, shown in Fig. 24(d) (black regions), were formed of solidified Cu10Sn phase mixed with partially un-melted Invar36 powder particles, rather than other types of defects including lack of fusion and inter-layer pores. VED of 208 J/mm^3 was also applied to the powder bed with 25 vol% Invar36 + 75 vol% Cu10Sn, and the resultant macrostructure and microstructure of the processed cross-sections was presented in Fig. 24(e) and (f). Some silver-coloured and irregular-shaped beads were found distributed on the solidified cross-section. These silver-coloured elements should be Fe and Ni from Invar36 due to their higher meting point. Unlike the case with 75 vol% Invar36, no distinct interfaces between the scanned layers could be observed. The mixed powder bed would have had a lower overall melting point and higher thermal conductivity as a result of the increased Cu10Sn content. Consequently, a good metallurgical bonding between layers could be obtained.

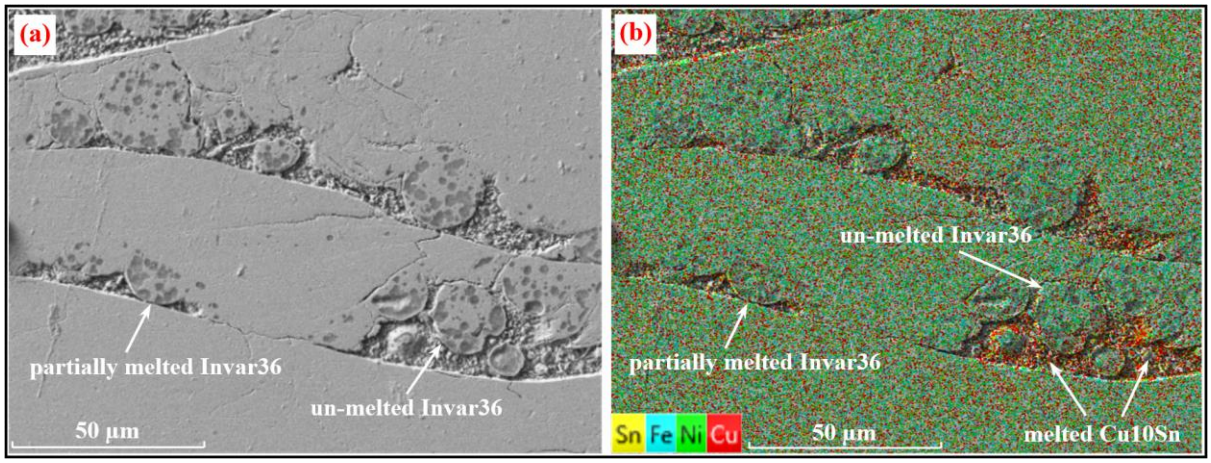

Fig. 25. (a) Microscopic image and (b) EDS mapping for 75 vol% Invar36 with 208 J/mm^3

An increased VED of 339 J/mm^3 (P = 285 W, v = 150 mm/s, h =140 µm and t = 40 µm) was applied to the powder mixture with 75 vol% Invar36. Defects including the embedded un-melted and partially melted powder particles became less distinct, as seen in Fig. 26(a) and (b). However, some interfaces between adjacent layers can still be observed, indicating that despite

having a higher VED, an increased hatch spacing can still lead to defects. This has a good agreement with the modelling results, which demonstrates that the hatch spacing plays an important role on the formation of defects.

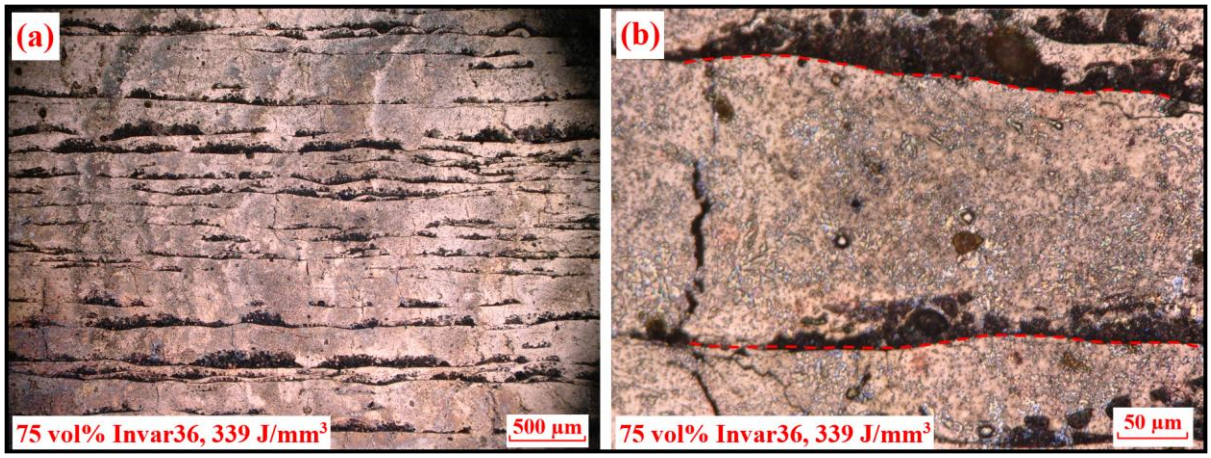

Fig. 26. (a) Microscopic image and (b) EDS mapping for 75 vol% Invar36 with 208 J/mm^3

6. Conclusions

Through numerical and experimental investigations, this study examines the mechanisms through which defects form during multi-material Invar36/Cu10Sn LPBF process. A DEM-CFD modelling framework was first employed to study the effects of powder mixture contents and process parameters on the track morphology, the development of molten pool and the formation of inter-layer/inter-track defects in the multi-material LPBF process. In addition, investigations into FGM with properties varying along the horizontal and vertical building directions were conducted. Samples with different Invar36 powder contents were fabricated with a multi-material LPBF system. Based on the modelling analysis and experimental observation, the conclusions can be drawn as follows:

- When increasing the content of Cu10Sn in the powder mixture, the temperature of the powder bed would decrease, resulting in a shallower molten pool depth for Invar36 powder. Consequently, defects would form including balling effect, isolated clusters

and partially/un-melted Invar36 powder particles embedded in the fully melted Cu10Sn phases. These defects could be eliminated by increasing the laser power.

- Inter-layer defects, including lack of fusion and irregular shaped pores, were more likely to occur with an increased layer thickness. The appearance of partially and un-melted Invar36 powder particles distributed on the lower level of the powder bed was related to low laser absorptivity, high thermal conductivity and low melting point of the Cu10Sn powder.
- The scanned track width first increased, and then decreased, when reducing the Invar36 content. As a result of the distinct thermal properties of the two powders, with a decreased Invar36 content, the track width was found to be related to an equilibrium between the laser absorptivity and thermal conductivity, as well as the overall melting point of the mixed powder bed. To avoid the inter-track defects, the hatch spacing should be optimised for each powder mixture with a different material composition.
- When processing FGM in the horizontal scanning direction, the process parameters should be adjusted along the scanning path to maintain a stable molten pool, and hence a continuous scanned track. For FGM processed in the vertical building direction, process parameters should be optimised for each layer with a different material content. In addition, each material content should be processed with multiple layers to avoid dilution.

A better understanding of the mechanisms through which defects form was obtained by conducting this study. Future work could include the investigation of microstructure evolution and mechanical behaviour for multi-material LPBF with different material contents, by incorporating the temperature development history with other modelling techniques, such as phase-field simulation and finite element analysis.

Acknowledgements

The authors appreciate The University of Manchester for providing the experimental samples. HG would like to thank the financial support of ASTUTE 2020 and ASTUTE East at Cardiff University. This work was also supported by the Natural Science Foundation of Jiangsu Province, China (grant number BK20190843); the Natural Science Foundation of the Jiangsu Higher Education Institutions of China (grant number 19KJB480002); Start-Up Foundation of Jiangsu University (20JDG057).

References

[1] J.P. Kruth, L. Froyen, J. Van Vaerenbergh, P. Mercelis, M. Rombouts, B. Lauwers, Selective laser melting of iron-based powder. Journal of Materials Processing Technology. (2004);149(1):616-22.

[2] K. Lin, Y. Fang, D. Gu, Q. Ge, J. Zhuang, L. Xi, Selective laser melting of graphene reinforced titanium matrix composites: Powder preparation and its formability. Advanced Powder Technology. (2021);32(5):1426-37.

[3] L. Thijs, F. Verhaeghe, T. Craeghs, J.V. Humbeeck, J.-P. Kruth, A study of the microstructural evolution during selective laser melting of Ti–6Al–4V. Acta Materialia. (2010);58(9):3303-12.

[4] C.Y. Yap, C.K. Chua, Z.L. Dong, Z.H. Liu, D.Q. Zhang, L.E. Loh, et al., Review of selective laser melting: Materials and applications. Applied physics reviews. (2015);2(4):041101.

[5] C. Wei, L. Li, X. Zhang, Y. Chueh, 3D printing of multiple metallic materials via modified selective laser melting. CIRP Annals. (2018);67(1):245-8.

[6] C. Zhang, F. Chen, Z. Huang, M. Jia, G. Chen, Y. Ye, et al., Additive manufacturing of functionally graded materials: A review. Materials Science and Engineering: A. (2019);764:138209.

[7] J. Chen, Y. Yang, C. Song, D. Wang, S. Wu, M. Zhang, Influence mechanism of process parameters on the interfacial characterization of selective laser melting 316L/CuSn10. Materials Science and Engineering: A. (2020);792:139316.

[8] Y. Bai, J. Zhang, C. Zhao, C. Li, H. Wang, Dual interfacial characterization and property in multi-material selective laser melting of 316L stainless steel and C52400 copper alloy. Materials Characterization. (2020);167:110489.

[9] K. Chen, C. Wang, Q. Hong, S. Wen, Y. Zhou, C. Yan, et al., Selective laser melting 316L/CuSn10 multi-materials: Processing optimization, interfacial characterization and mechanical property. Journal of Materials Processing Technology. (2020);283:116701.

[10] Z. Liu, D. Zhang, S. Sing, C. Chua, L. Loh, Interfacial characterization of SLM parts in multi-material processing: Metallurgical diffusion between 316L stainless steel and C18400 copper alloy. Materials Characterization. (2014);94:116-25.

[11] X. Mei, X. Wang, Y. Peng, H. Gu, G. Zhong, S. Yang, Interfacial characterization and mechanical properties of 316L stainless steel/inconel 718 manufactured by selective laser melting. Materials Science and Engineering: A. (2019);758:185-91.

[12] M. Zhang, Y. Yang, D. Wang, C. Song, J. Chen, Microstructure and mechanical properties of CuSn/18Ni300 bimetallic porous structures manufactured by selective laser melting. Materials & Design. (2019);165:107583.

[13] R. Wang, D. Gu, C. Chen, D. Dai, C. Ma, H. Zhang, Formation mechanisms of TiB2 tracks on Ti6Al4V alloy during selective laser melting of ceramic-metal multi-material. Powder Technology. (2020);367:597-607.
[14] S. Sing, L. Lam, D. Zhang, Z. Liu, C. Chua, Interfacial characterization of SLM parts in multi-material processing: Intermetallic phase formation between AlSi10Mg and C18400 copper alloy. Materials Characterization. (2015);107:220-7.
[15] C. Tey, X. Tan, S. Sing, W. Yeong, Additive manufacturing of multiple materials by selective laser melting: Ti-alloy to stainless steel via a Cu-alloy interlayer. Additive Manufacturing. (2020);31:100970.
[16] V.K. Nadimpalli, T. Dahmen, E.H. Valente, S. Mohanty, D.B. Pedersen, editors. Multi-material additive manufacturing of steels using laser powder bed fusion. Proceedings of the 19th International Conference and Exhibition; 2019: The European Society for Precision Engineering and Nanotechnology.
[17] C. Han, Y. Li, Q. Wang, D. Cai, Q. Wei, L. Yang, et al., Titanium/hydroxyapatite (Ti/HA) gradient materials with quasi-continuous ratios fabricated by SLM: Material interface and fracture toughness. Materials & Design. (2018);141:256-66.
[18] C. Wei, Z. Sun, Y. Huang, L. Li, Embedding anti-counterfeiting features in metallic components via multiple material additive manufacturing. Additive Manufacturing. (2018);24:1-12.
[19] Y. Chueh, X. Zhang, J.C. Ke, Q. Li, C. Wei, L. Li, Additive manufacturing of hybrid metal/polymer objects via multiple-material laser powder bed fusion. Additive Manufacturing. (2020);36:101465.
[20] J. Zhou, H. Li, Y. Yu, K. Firouzian, Y. Qian, F. Lin, Characterization of interfacial transition zone of functionally graded materials with graded composition from a single material in electron beam powder bed fusion. Journal of Alloys and Compounds. (2020);832:154774.
[21] M.G. Scaramuccia, A.G. Demir, L. Caprio, O. Tassa, B. Previtali, Development of processing strategies for multigraded selective laser melting of Ti6Al4V and IN718. Powder Technology. (2020);367:376-89.
[22] B. Rankouhi, S. Jahani, F.E. Pfefferkorn, D.J. Thoma, Compositional grading of a 316L-Cu multi-material part using machine learning for the determination of selective laser melting process parameters. Additive Manufacturing. (2021);38:101836.
[23] X. Zhang, Y.-h. Chueh, C. Wei, Z. Sun, J. Yan, L. Li, Additive manufacturing of three-dimensional metal-glass functionally gradient material components by laser powder bed fusion with in situ powder mixing. Additive Manufacturing. (2020);33:101113.
[24] X. Zhang, C. Wei, Y.-H. Chueh, L. Li, An Integrated Dual Ultrasonic Selective Powder Dispensing Platform for Three-Dimensional Printing of Multiple Material Metal/Glass Objects in Selective Laser Melting. Journal of Manufacturing Science and Engineering. (2018);141(1).
[25] C. Wei, Z. Sun, Q. Chen, Z. Liu, L. Li, Additive manufacturing of horizontal and 3D functionally graded 316L/Cu10Sn components via multiple material selective laser melting. Journal of Manufacturing Science and Engineering. (2019);141(8):081014.
[26] Y.-H. Chueh, X. Zhang, C. Wei, Z. Sun, L. Li, Additive Manufacturing of Polymer-Metal/Ceramic Functionally Graded Composite Components via Multiple Material Laser Powder Bed Fusion. Journal of Manufacturing Science and Engineering. (2020);142(5).
[27] J.L. Tan. Multiple material additive manufacturing platform: Nanyang Technological University; 2019.
[28] D. Dai, D. Gu, Tailoring surface quality through mass and momentum transfer modeling using a volume of fluid method in selective laser melting of TiC/AlSi10Mg powder. International Journal of Machine Tools and Manufacture. (2015);88:95-107.
[29] A. Sorkin, J.L. Tan, C.H. Wong, Multi-material modelling for selective laser melting. Procedia Engineering. (2017);216:51-7.
[30] H. Gu, C. Wei, L. Li, Q. Han, R. Setchi, M. Ryan, et al., Multi-physics modelling of molten pool development and track formation in multi-track, multi-layer and multi-material selective laser melting. International Journal of Heat and Mass Transfer. (2020);151:119458.

[31] Z. Sun, Y.-H. Chueh, L. Li, Multiphase mesoscopic simulation of multiple and functionally gradient materials laser powder bed fusion additive manufacturing processes. Additive Manufacturing. (2020):101448.
[32] C. Tang, J.L. Tan, C.H. Wong, A numerical investigation on the physical mechanisms of single track defects in selective laser melting. International Journal of Heat and Mass Transfer. (2018);126:957-68.
[33] W. Yan, W. Ge, Y. Qian, S. Lin, B. Zhou, W.K. Liu, et al., Multi-physics modeling of single/multiple-track defect mechanisms in electron beam selective melting. Acta Materialia. (2017);134:324-33.
[34] Q. Han, H. Gu, R. Setchi, Discrete element simulation of powder layer thickness in laser additive manufacturing. Powder Technology. (2019);352:91-102.
[35] D. Gu, M. Xia, D. Dai, On the role of powder flow behavior in fluid thermodynamics and laser processability of Ni-based composites by selective laser melting. International Journal of Machine Tools and Manufacture. (2019);137:67-78.
[36] EDEM. EDEM 2019 User Guide: DEM Solutions Ltd., Edinburgh, Scotland, UK. Copyright ©; 2018.
[37] H. Chen, W. Zhu, H. Tang, W. Yan, Oriented structure of short fiber reinforced polymer composites processed by selective laser sintering: The role of powder-spreading process. International Journal of Machine Tools and Manufacture. (2021);163:103703.
[38] W. Yan, Y. Qian, W. Ge, S. Lin, W.K. Liu, F. Lin, et al., Meso-scale modeling of multiple-layer fabrication process in Selective Electron Beam Melting: Inter-layer/track voids formation. Materials & Design. (2018);141:210-9.
[39] C. Qiu, N.J.E. Adkins, M.M. Attallah, Selective laser melting of Invar 36: Microstructure and properties. Acta Materialia. (2016);103:382-95.
[40] S. Scudino, C. Unterdörfer, K.G. Prashanth, H. Attar, N. Ellendt, V. Uhlenwinkel, et al., Additive manufacturing of Cu–10Sn bronze. Materials Letters. (2015);156:202-4.
[41] T. Gottwald, A. Neumann. Electronic sub-assembly, a method for manufacturing the same, and a printed circuit board with electronic sub-assembly. Google Patents; 2018.
[42] P. Carnavas, N. Page, Elastic properties of compacted metal powders. Journal of materials science. (1998);33(18):4647-55.
[43] N.D. Nikolić, S.B. Krstić, L.J. Pavlović, M.G. Pavlović, K.I. Popov, The mutual relation of decisive characteristics of electrolytic copper powder and effect of deposition conditions on them. Electroanalytical chemistry research trends Nova, New York. (2008):185-209.
[44] H. Chen, Q. Wei, Y. Zhang, F. Chen, Y. Shi, W. Yan, Powder-spreading mechanisms in powder-bed-based additive manufacturing: Experiments and computational modeling. Acta Materialia. (2019);179:158-71.
[45] H. Chen, Q. Wei, S. Wen, Z. Li, Y. Shi, Flow behavior of powder particles in layering process of selective laser melting: Numerical modeling and experimental verification based on discrete element method. International Journal of Machine Tools and Manufacture. (2017);123:146-59.
[46] S.M.H. Hojjatzadeh, N.D. Parab, W. Yan, Q. Guo, L. Xiong, C. Zhao, et al., Pore elimination mechanisms during 3D printing of metals. Nature Communications. (2019);10(1):3088.
[47] G.K. Batchelor. An Introduction to Fluid Dynamics. Cambridge: Cambridge University Press; 2000.
[48] V.R. Voller, A.D. Brent, C. Prakash, The modelling of heat, mass and solute transport in solidification systems. International Journal of Heat and Mass Transfer. (1989);32(9):1719-31.
[49] V.R. Voller, C. Prakash, A fixed grid numerical modelling methodology for convection-diffusion mushy region phase-change problems. International Journal of Heat and Mass Transfer. (1987);30(8):1709-19.
[50] C.W. Hirt, B.D. Nichols, Volume of fluid (VOF) method for the dynamics of free boundaries. Journal of Computational Physics. (1981);39(1):201-25.
[51] C. Jung-Ho, F.F. Dave, O.M. John, J.H. Kendall, Weld pool flows during initial stages of keyhole formation in laser welding. Journal of Physics D: Applied Physics. (2009);42(17):175502.

[52] J.I. Arrizubieta, A. Lamikiz, F. Klocke, S. Martínez, K. Arntz, E. Ukar, Evaluation of the relevance of melt pool dynamics in Laser Material Deposition process modeling. International Journal of Heat and Mass Transfer. (2017);115:80-91.
[53] A. Seifter, K. Boboridis, B. Didoukh, G. Pottlacher, P. Jäger, Thermophysical properties of liquid Fe64/Ni36 (INVAR®). J Chim Phys. (1997);94:1004-8.
[54] J. Brillo, I. Egry, Surface tension of nickel, copper, iron and their binary alloys. Journal of Materials Science. (2005);40(9):2213-6.
[55] Eclipse. ECLIPSE COMBUSTION ENGINEERING GUIDE. 8th, editor. United States of America: Eclipse, Inc.; 1986.
[56] Y. Kawai, M. Kishimoti, H. Tsuru, Surface Tension and Density of Liquid Cu-Sn Alloys. J Japan Inst Metals. (1973);37(6):668-72.
[57] C.D. Boley, S.A. Khairallah, A.M. Rubenchik, Calculation of laser absorption by metal powders in additive manufacturing. Appl Opt. (2015);54(9):2477-82.
[58] N. Chakraborty, The effects of turbulence on molten pool transport during melting and solidification processes in continuous conduction mode laser welding of copper–nickel dissimilar couple. Applied Thermal Engineering. (2009);29(17):3618-31.
[59] C. Tang, K.Q. Le, C.H. Wong, Physics of humping formation in laser powder bed fusion. International Journal of Heat and Mass Transfer. (2020);149:119172.
[60] R. Li, J. Liu, Y. Shi, L. Wang, W. Jiang, Balling behavior of stainless steel and nickel powder during selective laser melting process. The International Journal of Advanced Manufacturing Technology. (2012);59(9):1025-35.
[61] S.A. Khairallah, A.A. Martin, J.R.I. Lee, G. Guss, N.P. Calta, J.A. Hammons, et al., Controlling interdependent meso-nanosecond dynamics and defect generation in metal 3D printing. Science. (2020);368(6491):660.
[62] Q. Han, H. Gu, S. Soe, R. Setchi, F. Lacan, J. Hill, Manufacturability of AlSi10Mg overhang structures fabricated by laser powder bed fusion. Materials & Design. (2018);160:1080-95.
[63] L. Cao, Numerical simulation of the impact of laying powder on selective laser melting single-pass formation. International Journal of Heat and Mass Transfer. (2019);141:1036-48.
[64] R. Shi, S.A. Khairallah, T.T. Roehling, T.W. Heo, J.T. McKeown, M.J. Matthews, Microstructural control in metal laser powder bed fusion additive manufacturing using laser beam shaping strategy. Acta Materialia. (2020);184:284-305.
[65] C. Wei, Z. Sun, Q. Chen, Z. Liu, L. Li, Additive manufacturing of horizontal and 3D functionally graded 316L/Cu10Sn components via multiple material selective laser melting. Journal of Manufacturing Science and Engineering. (2019);141(8).
[66] L.D. Bobbio, R.A. Otis, J.P. Borgonia, R.P. Dillon, A.A. Shapiro, Z.-K. Liu, et al., Additive manufacturing of a functionally graded material from Ti-6Al-4V to Invar: Experimental characterization and thermodynamic calculations. Acta Materialia. (2017);127:133-42.
[67] Y. Sun, R. Bailey, A. Moroz, Surface finish and properties enhancement of selective laser melted 316L stainless steel by surface mechanical attrition treatment. Surface and Coatings Technology. (2019);378:124993.